Mammary ductal epithelium controls cold-induced adipocyte thermogenesis

Luis C. Santos[1,8], Douglas Arneson[2,5,8], Alexandra Alvarsson[1,8], Karthickeyan Chella Krishnan[3], Alessia Centzone[4], Sanil Patel[1], Shani Sadeh[1], In Sook Ahn[5], Graciel Diamante[5], Ingrid Cely[5], Atul J. Butte[2,6,7], Cédric Blanpain[5], Sarah A. Stanley[1], Aldons J. Lusis[3], Xia Yang[5], and Prashant Rajbhandari[1, 9]

[1]Diabetes, Obesity, and Metabolism Institute, Icahn School of Medicine at Mount Sinai, New York, NY USA
[2]Bakar Computational Health Sciences Institute, University of California, San Francisco, CA USA
[3]Department of Medicine/Division of Cardiology and Department of Human Genetics, University of California, Los Angeles, CA USA
[4]Laboratory of Stem Cells and Cancer, Université Libre de Bruxelles (ULB), Brussels, Belgium
[5]Department of Integrative Biology and Physiology and Bioinformatics Interdepartmental Program, University of California, Los Angeles, CA USA
[6]Department of Pediatrics, University of California, San Francisco, CA, USA
[7]Center for Data-Driven Insights and Innovation, University of California Health, Oakland, CA, USA

[8]Equal Contribution

[9]Corresponding author:

Prashant Rajbhandari PhD
Diabetes, Obesity, and Metabolism Institute
Department of Endocrinology and Bone Disease
Icahn School of Medicine at Mount Sinai
1 Gustave L. Levy Place
New York, NY 10029 USA
Office (212) 659-8653
E-mail: prashant.rajbhandari@mssm.edu

Main Figures: 4; Extended Data Figures: 4; Supplemental Movies: 2

ABSTRACT

Sympathetic activation during cold exposure increases adipocyte thermogenesis via expression of mitochondrial protein uncoupling protein 1 (UCP1)[1]. The propensity of adipocytes to express UCP1 is under a critical influence of the adipose microenvironment and varies among various fat depots[2-7]. Here we report that cold-induced adipocyte UCP1 expression in female mouse subcutaneous white adipose tissue (scWAT) is regulated by mammary gland ductal epithelial cells in the adipose niche. Single cell RNA-sequencing (scRNA-seq) show that under cold condition glandular alveolar and hormone-sensing luminal epithelium subtypes express transcripts that encode secretory factors involved in regulating adipocyte UCP1 expression. We term mammary duct secretory factors as "mammokines". Using whole-tissue immunofluorescence 3D visualization, we reveal previously undescribed sympathetic nerve-ductal points of contact and show that sympathetic nerve-activated mammary ducts limit adipocyte UCP1 expression via cold-induced mammokine production. Both *in vivo* and *ex vivo* ablation of mammary ductal epithelium enhances cold-induced scWAT adipocyte thermogenic gene program. The mammary duct network extends throughout most scWATs in female mice, which under cold exposure show markedly less UCP1 expression, fat oxidation, energy expenditure, and subcutaneous fat mass loss compared to male mice. These results show a previously uncharacterized role of sympathetic nerve-activated glandular epithelium in adipocyte thermogenesis. Overall, our findings suggest an evolutionary role of mammary duct luminal cells in defending glandular adiposity during cold exposure, highlight mammary gland epithelium as a highly active metabolic cell type, and implicate a broader role of mammokines in mammary gland physiology and systemic metabolism.

60 **MAIN**

61 The scWAT depots in female mice are mostly mammary gland WATs (mgWAT) which is highly
62 heterogenous tissue consisting of adipocytes, preadipocytes, mesenchymal stem cells, immune
63 cells, endothelial cells, SNS nerve fibers, and mammary epithelial cells forming a ductal structure.
64 The epithelial cells are divided into myoepithelial/basal cells, and luminal cells, which can be
65 luminal hormone sensing, or not[8]. In virgin female mice, the mammary gland already has ductal
66 structures in the anterior and posterior scWAT and metabolic cooperativity between luminal ductal
67 cells and stroma is known to be important for mammary gland function and development[8,9].
68 Profound changes in mammary ducts and adipocytes are seen during gestation, pregnancy,
69 lactation, and post-involution[10,11]. The importance of adipocytes for mammary duct
70 morphogenesis, the dedifferentiation of adipocytes during lactation, and reappearance during
71 lactation post-involution, all suggest a dynamic homeostatic interplay between ductal luminal
72 epithelial cells and adipocytes[11-13]. It is not clear, however, what paracrine signaling programs
73 from mammary ducts regulate adipocyte metabolism and thermogenesis. Notably, our current-
74 state-of knowledge of WAT thermogenesis and UCP1 expression is mostly based on male
75 scWATs, which lacks mammary glandular epithelial cells. Importantly, besides the role of
76 immune cells in the adipose microenvironment, the contribution of other cell types in controlling
77 adipocyte UCP1 expression is still not clear.

78 To study cellular heterogeneity, inter-tissue communication, and cellular transcription
79 dynamics in mgWAT in a thermogenic condition, we isolated the stromal vascular fraction (SVF)
80 from the mgWAT of 10-week-old virgin female mice exposed to 24-hour cold (COLD, 4ºC) or
81 room temperature (RT) and performed scRNA-seq (Fig. 1A). We obtained 12,222 cells and used
82 Cell Ranger software from 10X Genomics for data processing and the R package Seurat[14] to

83 generate cell clusters and resolve their identities as previously described[15] (see Methods). We
84 integrated our dataset with eight other publicly available single cell datasets, from mammary gland
85 tissues including *Tabula Muris* and *Tabula Muris Senis*[16-19] : i) for cell type identification, ii) to
86 increase confidence in the projected cell type, iii) for sex and age differences, and iv) for mammary
87 gland development (Extended Data Fig. 1A, and Table 1). This integrated dataset allowed us to
88 precisely annotate various cell types present in mgWAT of female mice. Further subclustering of
89 our integrated dataset based on known cell type marker genes identified clusters of a) adipocyte
90 precursor cells (APCs), b) B cells, c) macrophages, d) T cells, e) endothelial cells, f) immune
91 precursor cells (IPC), g) dendritic cells (DC) , h) Schwann cells, i) myoepithelial cells (myoep),
92 and j) luminal-hormone sensing (Luminal-HS), luminal-alveolar (Luminal -AV), luminal-HS-AV,
93 and myoepithelial cells (Fig. 1B, Extended Data Fig. 1B and 1C).

94 To gain insight into the remodeling of stromal cells under adrenergic stress, we segregated
95 the cumulative tSNE-plot into RT and COLD treatment by animal replicate. The tSNE and dot
96 plots reveal global changes in relative proportions of SVF clusters between RT and COLD (Fig.
97 1C). Among all the clusters luminal cells showed significant differences in cell type percentages
98 (RT 1:7.2%, RT 2: 7.5%; COLD 1: 16.9%, COLD 2: 19.1%) and appeared to have large
99 differences in their global transcriptomic profiles in the t-SNE two-dimensional projection where
100 cells from RT and COLD were segregated (Fig. 1C). To quantitatively determine the
101 transcriptional impact of cold treatment on individual cell types, we characterized differentially
102 expressed genes as a function of cluster types and found a high degree of transcriptional variation
103 in luminal HS and AV under the cold conditions (Extended Data Fig. 1D). Further subclustering
104 of luminal epithelial cell types (luminal HS, luminal AV, and luminal HS-AV) revealed marked
105 differences in clustering at RT and COLD [20] (Fig. 1C and Extended Data Fig. 1D, 1E).

106 Luminal cell clusters showed remarkable transcriptional differences in cell clusters
107 between RT and cold, implicating a potential remodeling of the luminal epithelium upon cold
108 exposure (Fig. 1C, 1D and Extended Data Fig. 1D-1F). To probe for factors that are differentially
109 expressed in luminal cells under cold exposure, we performed differential gene expression (DEG)
110 analysis on RT and cold exposed luminal subclusters. We found upregulation of *Wnt4*, Adropin
111 (*Enho*), leucine rich alpha-2 glycoprotein (*Lrg1*), Diglyceride acyltransferase (*Dgat2*), haptoglobin
112 (*H*p), and angiopoietin-like 4 (*Angptl4*) in Luminal HS cells, lipocalin-2 (*Lcn2*), *Angptl4*, and
113 Apolipoprotein B editing complex (*Apobec3*) in Luminal AV cells, and *Lrg1*, neuregulin 4 (*Nrg4*),
114 ceruloplasmin (*Cp*), *Angptl4* in Luminal HS-AV cells (Fig. 1E-1G, Extended Data Fig. 1G). Many
115 of these genes (shown by red arrows in Fig. 1E-1G) encode secreted factors that play important
116 roles in local and systemic lipid metabolism[21-30]. t-SNE plots of normalized gene expression levels
117 for cold-induced mammokines in mgWAT (our study), male scWAT SVFs and mature
118 adipocytes[31] show that *Angptl4* is also expressed by most mature adipocytes; however, other cold-
119 induced mammokine genes showed relatively localized expression in ductal epithelial cell
120 adhesion molecule (*Epcam)*+ cells (Extended Data Fig. 1G and 1H). Our RNAscope fluorescent
121 in situ hybridization (FISH) analysis showed a highly localized expression of mammokines *Enho,*
122 *Mfge8, Lrg1, Lcn2, Hp, Nrg4,* and *Wnt4* in *Epcam*+ and *Krt8*+ (luminal ductal epithelial markers)
123 in mammary ductal luminal cells (Fig. 1H).
124 Shifts in the luminal epithelium transcriptomic state with cold and localized expression of
125 beta-adrenergic receptors, *Adrb2* and *Adrb1* expression in luminal cells, suggests that these cells
126 may directly respond to cold-induced SNS activation[32-34] (Fig. 1C and Extended Data Fig. 1G). To
127 determine if duct epithelial cells are innervated by sympathetic nerves, we used Adipoclear, a
128 robust protocol based on immunolabeling-enabled three-dimensional imaging of solvent-cleared

129 organ iDISCO (22), for high-resolution, three-dimensional imaging of mammary tissue. We
130 analyzed the 3D distribution and density of a sympathetic marker, tyrosine hydroxylase (TH), and
131 its relationship to EPCAM+ mammary ductal cells in mgWAT from mice exposed to RT or cold.
132 Cold exposure caused prominent morphological changes in mammary ducts such as increased
133 EPCAM+ branching and terminal ductal bifurcations (Fig. 2A and Extended Data Fig. 2A), which
134 is consistent with data showing increased branch morphogenesis upon isoproterenol treatment[35].
135 Our data further reveal that nerve fibres are interwoven with mammary gland ducts and alveolar
136 structures in mgWATs (Supplementary Movie 1). However, we did not see an effect of cold
137 treatment on duct volume, nerve volume, or the ratio of duct-to-nerve volume (Fig. 2B). To
138 examine interactions between sympathetic innervation and mammary gland ducts in more detail,
139 we performed confocal imaging in six regions of the mgWAT fat pad from each of 6 RT and 6
140 cold-treated mice. Consistent with our scRNA-seq data, we saw a significant increase in EPCAM
141 staining in the ducts of cold-exposed mgWAT (Fig 2C and 2D). We also identified contacts
142 between TH+ fibres and EPCAM+ ducts (neuroductal points) with a trend to increased volume of
143 nerve contacts (normalized for duct volume) in cold-treated mice ($p = 0.09$, Fig S2F). Interestingly,
144 TH intensity, which has been reported to increase with sympathetic activation, was significantly
145 higher at the neuroductal points in cold exposed mgWAT compared to controls (Fig 2C, 2E, 2F
146 Supplementary Movie 2). Similarly, EPCAM intensity was also significantly elevated at
147 neuroductal points in keeping with local induction of expression. However, there were no
148 significant changes in duct or nerve volume or in TH intensity across the whole nerve volume
149 (Extended Data Fig 2C-2H). Taken together, our data show a significant remodelling of mammary
150 ducts and their contacts with sympathetic innervation upon cold exposure.

151 To explore the biological relevance of cold-induced increase in i) luminal subtype
152 population transcriptional state (Fig. 1) and ii) EPCAM intensity and SNS innervation of
153 mammary ducts (Fig. 2), we first purified EPCAM+ and EPCAM- cells from mgWAT of RT and
154 cold-exposed mice and then stained for EPCAM and CD49F for fluorescence-activated cell sorting
155 (FACS) analysis to probe for luminal cell population changes under cold stress. As shown in
156 Extended Data Fig. 3A, we noticed three distinct populations of cells that were $EPCAM^{lo}CD49F^{lo}$
157 (stromal), $EPCAM^{hi}CD49F^{hi}$ (luminal), and $EPCAM^{lo}CD49F^{hi}$ (basal) cells. Luminal cells were
158 only enriched in EPCAM+ purified cells and showed a cold-dependent increase in cell population
159 compared to RT conditions. We also noticed a marked reduction in the basal cell population upon
160 cold treatment in EPCAM+ selected cells, consistent with the scRNA-seq data in Fig. 1C
161 (myoepithelial cluster, RT: 2.15%, COLD: 0.65%). These data indicate a differential response to
162 cold stress by luminal and basal cells in ducal epithelium (Extended Data Fig. 3A). To test whether
163 luminal cells directly responded to SNS activation, we tested mammokine expression in isolated
164 primary EPCAM+ mgWAT that were either treated or not treated with isoproterenol. Cold-induced
165 mammokines showed increased expression upon isoproterenol (beta-adrenergic receptor agonist)
166 treatment (Extended Data Fig. 3B). To determine whether adrenergic-activated luminal cells are
167 involved in mgWAT adipose thermogenesis, we depleted EPCAM+ cells from mgWAT SVFs by
168 positive selection using magnetic cell sorting (MACS) and differentiated SVFs *ex vivo* with and
169 without ductal cells into beige adipocytes (Fig. 3A). Depletion of EPCAM+ cells from SVFs of
170 RT mgWAT potentiated expression of thermogenic genes such as *Ucp1*, *Cox8b, Ppargc1a* and
171 *Cidea* and this potentiation of thermogenic genes was markedly amplified in the cold-exposed
172 condition (Fig. 3A and Extended Data Fig 3C). To further test the crosstalk of epithelial cells and
173 adipocytes, we developed an *in vitro* co-culture system involving a controlled mixture of

174 adipogenic 10T1/2 cells with nontransformed mouse mammary gland (NMuMG cells) (derived
175 from "normal" mammary epithelium). Seeding density of as low as 2.5% NMuMG cells resulted
176 in a significant reduction of *Ucp1* and beiging potential of 10T1/2 cells compared to the pure
177 culture (Fig. 3B and Extended Data Fig. 3D-3F). The higher the fraction of NMuMG cells in the
178 co-culture, the lower the relative expression of *Ucp1* and other thermogenic genes such as *Cox8B*
179 and *Ppargc1a* measured by RT-qPCR (Fig. 3B). To test the *ex vivo* and *in vivo* role of ductal
180 epithelial cells in adipose thermogenesis, we compared aged-matched female mgWAT with three
181 complimentary ductal ablated models; i) estrogen receptor-alpha (ERa) knockout mice (*Esr1* KO),
182 ii) male mice which lack or possess only rudimentary glandular ducts, iii) inguinal (ducts) or
183 dorsolumbar (no ducts) portion of mgWAT from 5-week-old female mice. First, to test the role of
184 ductal cells in adipose thermogenesis, we isolated SVFs from male iWATs and female mgWATs
185 and differentiated them into beige adipocytes in the presence or absence of isoproterenol. We
186 found that SVFs from male iWATs show markedly higher beiging and isoproterenol-mediated
187 *Ucp1* expression compared to EPCAM+ SVFs from female mgWAT (Fig. 3C and Extended Data
188 Fig. 3G). In agreement with the ex vivo data, female mgWATs showed significantly less
189 expression of cold-induced thermogenic genes such as *Ucp1*, *Cox8b,* and *Ppargc1a* compared to
190 male iWATs (Fig. 3D). Since mgWATs make up almost all of the subcutaneous fat mass in female
191 mice, we reasoned that highly reduced adipocyte thermogenic gene expression could potentially
192 influence whole body energy metabolism. To test this, we performed indirect calorimetry on age-
193 matched male and female mice at RT and 24 hr cold exposure using a metabolic chamber. We
194 found that female mice showed highly reduced energy expenditure (EE), oxygen consumption
195 (VO2), and carbon dioxide production (VCO2) during cold exposure compared to male mice (Fig.
196 3E and Extended Data Fig. 3I). Female mice showed markedly higher respiratory exchange ratio

197 (RER) than males under cold exposure, indicating a decrease in cold-induced fat oxidation and the
198 possibility that mgWATs maintain adiposity under cold stress (Fig. 3E and Extended Data Fig.
199 3J). Generalized linear model (GLM)-based regression analyses showed a significant group and
200 interaction effect in RER between males and females based on fat mass as a covariate (Extended
201 Data Fig. 3J). We did not see significant differences in locomotor activities and food consumption
202 between the sexes (Extended Data Fig. 3K). These RER data were further supported by our
203 magnetic resonance imaging (MRI) body composition analysis which showed that male mice lose
204 significant body weight and fat mass during cold stress whereas females show no differences
205 before and after cold stress (Fig.3F and Extended Data Fig. 3H). Next, we compared the cold-
206 induced thermogenic gene expression program between WT and Estrogen Receptor-alpha (*Esr1*
207 KO) mice. *Esr1* KO mice are known to possess hypoplastic mammary ducts and remain
208 rudimentary throughout the life span of a female mouse[36]. As shown in Fig. 3G, cold-exposed *Esr1*
209 KO mice showed markedly increased expression of *Ucp1,* and other thermogenic genes compared
210 to WT control. In the 5 weeks after birth, mammary ducts are concentrated in the inguinal portion
211 closer to the nipple and are confined near the lymph node and virtually absent toward the
212 dorsolumbar region of the mgWAT, providing distinct anatomical regions within the mgWAT to
213 test the role of ductal epithelium in adipose thermogenesis[37]. 5-week-old female mice were
214 exposed to cold and inguinal and dorsolumbar regions were dissected to assess thermogenic
215 transcripts. *Epcam* transcripts were present only in the inguinal region, however, thermogenic
216 genes were mostly similar between inguinal and dorsolumbar region except for *Ucp1* where we
217 saw an increase in *Ucp1* levels in inguinal part (Fig. 3H). Chi et. al reported regional differences
218 between inguinal and dorsolumbar region and there could be a regional control of *Ucp1* expression
219 in 5-week-old mice independent of ductal cells[38]. However, consistent with our data, we noticed

220 significantly less expression of genes involved in lipid mobilization such as *Pnpla2* and *Hsl,* in
221 inguinal regions compared to dorsolumbar, indicating that the ductal epithelium is potentially
222 inhibiting cold-induced lipid mobilization. All these data point, for the first time, toward a possible
223 unique mechanism of SNS-activated mgWAT under cold stress to limit thermogenesis and
224 preserve adiposity.

225 Our results show a unique possible SNS-mediated crosstalk between mammary ductal cells
226 and adipocytes to control adipocyte thermogenesis. Our differentially expressed genes in
227 mammary ductal cells under adrenergic stimulation showed upregulation of genes that encode
228 factors such as Angptl4*,* Enho, Lrg1, and Lcn2, which are known to play inhibitory roles in
229 adipocyte thermogenesis. These factors also showed high enrichment in mammary *Epcam*+ cells
230 by scRNA-seq and RNAscope in situ hybridization. Among these factors, *Lcn2* was previously
231 shown to inversely correlate with *Ucp1* expression in female gonadal WAT (gWAT)[24]. Female
232 gWATs, which lack mammary ducts, express exceedingly high levels of *Ucp1* compared to male
233 gWATs[24]. Reciprocally, we find that cold-stressed female mgWATs express high levels of *Lcn2*
234 and low levels of *Ucp1* compared to males (Fig. 3D and Extended Data Fig. 4A). The secretion of
235 Lcn2 by luminal AV and HS-AV cells could potentially be a mechanism of luminal cells to block
236 excess thermogenesis and preserve adiposity. Consistent with data in Fig.1 and Fig.3, both
237 isoproterenol treatment and cold exposure led to an increase in *Lcn2* levels in *Epcam*+ mammary
238 ducts (Extended Data Fig. 4B). To test adrenergic-dependent expression of Lcn2 protein
239 expression in luminal cells, we used organoids from a genetic mouse model that is based on
240 doxycycline (Dox)-based tet-responsive diphtheria toxin A (DTA) system derived from
241 interbreeding two transgenic strains: (1) mice expressing the tetracycline-on (''tet-on'')
242 transcription factor rtTA under the control of the luminal epithelial cell-specific *Krt8* gene

243 promoter (K8rtTA); (2) mice expressing tet-responsive DTA (TetO-Cre) that can be activated in
244 the presence of Dox. This model enables luminal cell ablation in a temporally regulated manner.
245 Mammary duct organoids isolated from *K8*rtTA-DTA mice[39] show increases in Lcn2 protein
246 expression upon isoproterenol treatment and these increases were diminished upon Dox treatment
247 (Fig. 4A and Extended Fig. 4C-4H), showing a direct response of luminal cells to produce Lcn2.
248 To test the physiological role of Lcn2 in regulating mgWAT thermogenesis, we mimicked cold
249 induction of Lcn2 production in mgWAT by inducing Lcn2 exogenous expression specifically in
250 mgWAT of *Lcn2* KO mice by injecting adipoAAV-Lcn2 or adipoAAV-GFP[24] (See Methods). Our
251 unbiased bulk RNA-seq data from the mgWATs of adipoAAV-Lcn2 injected mice show that *Lcn2*
252 expression was not supraphysiological compared to controls (Fig. 4B). The volcano plot in Fig.
253 4B demonstrates that Lcn2 exogenous expression significantly decreased the expression of
254 thermogenic genes such as *Ucp1, Cidea, Ppara* and increased expression of adipogenic genes
255 including *Lep, Mmp12*[40,41], *Zfp423*[42], and Lbp[43]. Lcn2 overexpression also led to an increase in
256 *Aldh1a1,* which was recently shown to inhibit adipose thermogenesis by downregulating UCP1
257 levels[44,45]. We validated our RNA-seq data by directed qPCR in both Lcn2 reconstituted mgWAT
258 of *Lcn2* KO and WT mice (Fig. 4C) and treated beige differentiated SVFs isolated from *Lcn2* KO
259 mgWATs with and without recombinant Lcn2 (Extended Data Fig. 4I). Finally, to test the role of
260 Lcn2 under cold stress, female *Lcn2* KO and WT mice were exposed to cold (4°C) for 24 hr.
261 Compared to controls, cold-exposed *Lcn2* KO mice mgWAT showed more beiging/browning and
262 gene expression analysis showed a significant increase in thermogenic genes such as *Ucp1*
263 indicating that Lcn2 is potentially one of the limiting factors involved in regulating the propensity
264 of mgWAT to beige (Extended Data Fig. 4J). Overall, our scRNA-seq analysis and both our tissue-
265 specific gain-of-function and loss-of-function experimental data show Lcn2 as a factor expressed

266 in luminal cells that could function to inhibit thermogenesis and maintain adiposity in mgWAT
267 during cold-stress.

268 In summary, our studies have uncovered a direct inhibitory role of mammary duct luminal
269 cells in adipocyte *Ucp1* expression and thermogenic gene program. SNS fibers directly innervate
270 EPCAM+ luminal cells and adrenergic stimulation of luminal cells transduce expression of
271 mammokines such LCN2 that regulates *Ucp1* expression in mgWAT adipocytes under cold
272 exposure. Depletion of EPCAM+ luminal epithelial cells potentiate the capacity of ex vivo
273 differentiated mgWAT preadipocytes to express UCP1, and female mice with ductal epithelium
274 loss show higher cold-induced UCP1 expression compared to controls. Importantly, female mice
275 demonstrate significantly less scWAT adipocyte UCP1 expression compared to male mice under
276 cold exposure. Taken together, these findings provide a new insight into mammary gland biology,
277 expand our understanding of the role of adipose microenvironment in adipocyte UCP1 expression,
278 and reveal the potential of mammokines to regulate local and systemic energy homeostasis.
279

280 **METHODS**

281 **Animal Studies**

282 C57BL/6 WT male and female mice (#000664), *ESR1* KO (#004744), LCN2KO (#24630) were
283 acquired from Jackson Laboratory and maintained in a pathogen-free barrier-protected
284 environment (12:12 h light/dark cycle, 22°C-24°C) at the UCLA and Mount Sinai animal facilities.
285 The Krt8rtTA-TetO-DTA mouse model was described previously[39]. For the time course cold
286 exposure experiment, WT mice at 8-10 weeks of age were singly housed at 4°C room in a non-
287 bedded cage without food and water for first 6 h; thereafter food, water, and one cotton square
288 were added. For the 24 h harvest, 3 h before harvest, food, water, and cotton square were removed

289 and then mice were harvested. At the end of the experiment, mgWATs were resected for analysis.
290 For overexpression studies, recombinant adeno-associated virus serotype 8 (AAV8) expressing
291 LCN2 or GFP was generated and injected as described previously[24]. Indirect calorimetry was
292 performed using Promethion Systems (Sable Systems, Las Vegas, NV). Animals were placed
293 individually in chambers at ambient temperature (22.0 °C) for 21 hr followed by 24 hr cold (4.0
294 °C) with 12 hr light/dark cycles. Animals had free access to food and water. Respiratory
295 measurements were made in 5 min intervals after initial 7-9 hr acclimation period. Energy
296 expenditure was calculated from VO2 and RER using the Lusk equation, EE in Kcal/hr = (3.815
297 + 1.232 X RER) X VO2 in ml/min. Indirect calorimetry data were analyzed by CALR web-based
298 software[46]. Body composition (fat mass) was determined using EchoMRI Body Composition
299 Analyzer. Animal experiments were conducted in accordance with the Mount Sinai and UCLA
300 Institutional Animal Care and Research Advisory Committee.
301
302 **RNA-Seq**
303 RNA isolation, library preparation, and analysis were conducted as previously described[24]. Flash-
304 frozen mgWAT samples were homogenized in QIAzol (Qiagen, Germantown, MD), and following
305 chloroform phase separation, RNA was isolated according to the manufacturer's protocol using
306 miRNeasy columns (Qiagen, Germantown, MD). Libraries were prepared from extracted mgWAT
307 fat RNA (Agilent 2200 Tapestation eRIN >8.2) using KAPA Stranded mRNA-Seq Kit (cat
308 #KK8421, KAPA Biosystems, Wilmington, MA), per the manufacturers' instructions. The pooled
309 libraries were sequenced using an Illumina HiSeq4000 instrument with SE50bp reads (Illumina,
310 San Diego, CA). Reads were aligned to the mouse genome mm10 using STAR[47] or HISAT2[48]
311 aligner and quantified using the Bioconductor R packages as described in the RNA-Seq

312 workflow[49]. *P* values were adjusted using the Benjamini-Hochberg procedure of multiple
313 hypothesis testing[49].
314
315 **Single cell isolation from SVF**
316 Single cell SVF populations from adipose tissue were isolated as described previously[3,31]. The
317 fourth inguinal white adipose tissue (iWAT) depot mgWAT from mice exposed to cold stress
318 (4°C) or room temperature for 24 hr was dissected and placed on a sterile 6-well tissue culture
319 plate with ice-cold 1X DPBS. Excess liquid was removed from fat pads by blotting. Each tissue
320 was cut and minced with scissors and then placed in 15 ml conical tubes containing digestion
321 buffer (2 ml DPBS and Collagenase II at 3 mg/ml; Worthington Biochemical, Lakewood, NJ,
322 USA) for 40 min of incubation at 37°C with gentle shaking at 100 rpm. Following tissue digestion,
323 enzyme activity was stopped with 8 ml of resuspension media (DMEM/F12 with glutamax
324 supplemented with 15%FBS and 1% pen/strep; Thermo Scientific, CA). The digestion mixture
325 was passed through 100 µm cell strainer and centrifuged at 150 x g for 8 min at room temperature.
326 To remove red blood cells, the pellet was resuspended and incubated in RBC lysis buffer (Thermo
327 Scientific, CA) for 3 min at room temperature, followed by centrifugation at 150 x g for 8 min.
328 The pellet was then resuspended in resuspension media and again spun down at 150 x g for 8 min.
329 The cell pellet was resuspended in 1 ml of 0.01% BSA (in DPBS) and passed through a 40 µm cell
330 strainer (Fisher Scientific, Hampton, NH, USA) to discard debris. Cell number was counted for
331 10X Genomics single cell application.
332
333 **SVF single cell barcoding and library preparation**

334 To yield an expected recovery of 4000-7000 single cells, an estimated 10,000 single cells per
335 channel were loaded onto Single Cell 3' Chip (10X Genomics, CA). The Single Cell 3' Chip was
336 placed on a 10X Genomics instrument to generate single cell gel beads in emulsion (GEMs).
337 Chromium Single Cell 3' v3 Library and Cell Bead Kits were used according to the manufacturer's
338 instructions to prepare single cell RNA-Seq libraries.
339
340 **Illumina high-throughput sequencing libraries**
341 Qubit Fluorometric Quantitation (ThermoFisher, Canoga Park, CA, USA) was used to quantify
342 the 10X Genomics library molar concentration and a TapeStation (Aligent, Santa Clara, CA, USA)
343 was used to estimated library fragment length. Libraires were pooled and sequenced on an Illumina
344 HiSeq 4000 (Illumina, San Diego, CA, USA) with PE100 reads and an 8 bp index read for
345 multiplexing. Read 1 contained the cell barcode and UMI and read 2 contained the single cell
346 transcripts.
347
348 **Single cell data pre-processing and quality control**
349 To obtain digital gene expression matrices (DGEs) in sparse matrix representation, paired end
350 reads from the Illumina HiSeq 4000 were processed and mapped to the mm10 mouse genome
351 using 10X Genomics' Cell Ranger v3.0.2 software suite. Briefly, .bcl files from the UCLA Broad
352 Stem Cell Research Center sequencing core were demultiplexed and converted to fastq format
353 using the 'mkfastq' function from Cell Ranger. Next, the Cell Ranger 'counts' function mapped
354 reads from fastq files to the mm10 reference genome and tagged mapped reads as either exonic,
355 intronic, or intergenic. Only reads which aligned to exonic regions were used in the resulting
356 DGEs. After combining all four sample DGEs into a single study DGE, we filtered out cells with

357 (1) UMI counts < 700 or > 30,000, (2) gene counts < 200 or > 8,000, and (3) mitochondrial gene
358 ratio > 10%. This filtering resulted in a dataset consisting of 42,052 genes across 12,222 cells, with
359 approximately 2,300 – 4,650 cells from each sample. A median of 2,411 genes and 7,252
360 transcripts were detected per cell.
361

362 **Identification of cell clusters**

363 To achieve high resolution cell type identification and increased confidence in our cell type
364 clustering we brought in external publicly available single cell data from SVF and mammary
365 tissues. Specifically, we included single cell data from 9 datasets comprising 91,577 single cells
366 from the mammary gland and multiple adipose depots, across 4 different single cell platforms
367 (**Table 1**). These external datasets and the SVF data from this study were all independently
368 normalized using sctransform[50] and integrated using Seurat[51,52] v3.1.5. The single cell expression
369 profiles were projected into two dimensions using UMAP[53] or tSNE[54] and the Louvain[55] method
370 for community detection was used to assign clusters. This integrated data was only used to identify
371 and define the cell types. All plots which are not explicitly designated as integrated with at least
372 one external dataset and all downstream analyses (e.g. differential expression analyses) were
373 conducted on non-integrated data to retain the biological effect of the cold treatment. Visualization
374 of the non-integrated data was conducted on a subsampled dataset where all samples had the same
375 number of cells to give an equal weight to each sample, however, all downstream analyses (e.g.
376 differential expression analyses) leveraged the full dataset.

Cell #	Tissue	Sex	Condition	Technology	Name	Source
22,800	BAT, EPI, ING)	M	SVF	Drop-Seq	Broad SVF	Broad Single Cell Portal[56]

25,010	Mammary	F	NP, G, L, PI	10X Genomics	MammaryEpi	GSE106273[57]
14,927	Mammary	F	NP, G, L, PI	Microwell-seq	MouseCellAtlas	figshare[58,59]
4,481	Mammary	F	N/A	10X Genomics	TM.Mammary.10X	figshare[17,60]
2,405	Mammary	F	N/A	FACS + Smart-seq2	TM.Mammary.FACS	figshare[17,60]
4,967	SVF (BAT, GAT, MAT, SCAT)	F, M	N/A	FACS + Smart-seq2	TM.SVF.FACS	figshare[17,60]
3,132	Mammary	F	Age (3m, 18m, 21m)	FACS + Smart-seq2	TS.Mammary.FACS	figshare[18,61]
5,080	SVF (BAT, GAT, MAT, SCAT)	F, M	Age (18m, 21m, 30m)	10X Genomics	TS.SVF.10X	figshare[18,61]
8,775	SVF (BAT, GAT, MAT, SCAT)	F, M	Age (3m, 18m, 24m)	FACS + Smart-seq2	TS.SVF.FACS	figshare[18,61]

Table 1: Publicly available single cell datasets used in this study

BAT – brown adipose tissue, EPI – epididymal white adipose tissue, ING – inguinal white adipose tissue, NP - nulliparous, G - gestation, L – lactation, PI - post involution, GAT – gonadal adipose tissue, MAT – mesenteric adipose tissue, SCAT – subcutaneous adipose tissue

Cell type-specific gene expression signatures

Cell type-specific gene expression signatures were generated by identifying genes with expression levels two-fold greater (adjusted p-values < 0.05) than all other cell types. To ensure consistency across samples, Seurat's FindConservedMarkers function (Wilcoxon rank sum test with a meta p-value) was applied across each sample.

388

389 **Resolving cell identities of the cell clusters**

390 To identify the cell type identity of each cluster, we used a curated set of canonical marker genes
391 derived from the literature (**Supplementary Table 1**) to find distinct expression patterns in the
392 cell clusters. Clusters which uniquely expressed known marker genes were used as evidence to
393 identify that cell type. Cell subtypes which did not express previously established markers were
394 identified by general cell type markers and novel markers obtained with Seurat's
395 FindConservedMarkers function were used to define the cell subtype.

396

397 **Differential gene expression analysis**

398 Within each identified cell type, cold treated and room temperature single cells were compared for
399 differential gene expression using Seurat's FindMarkers function (Wilcoxon rank sum test) in a
400 manner similar to Li et al.[19]. Differentially expressed genes were identified using two criteria: (i)
401 an expression difference of >= 1.5-fold and adjusted p-value < 0.05 in a grouped analysis between
402 room temperature mice (n = 2) and cold treated mice (n = 2); (ii) an expression difference of >=
403 1.25 fold and consistent fold change direction in all 4 possible pairwise combinations of cold-
404 treated vs room temperature mice.

405

406 **Pathway enrichment analysis**

407 Pathway enrichment analysis was conducted on the differentially expressed genes from each cell
408 type using gene sets from KEGG[62], Reactome[63], BIOCARTA[64], GO Molecular Functions[65], and
409 GO Biological Processes[65]. Prior to enrichment, mouse gene names were converted to human
410 orthologues. Enrichment of pathways was assessed with a Fisher's exact test, followed by multiple

411 testing correction with the Benjamini-Hochberg method. Gene set enrichments with FDR < 0.05
412 were considered statistically significant.
413
414 **Real time qPCR**
415 Total RNA was isolated using TRIzol reagent (Invitrogen) and reverse transcribed with the iScript
416 cDNA synthesis kit (Biorad). cDNA was quantified by real-time PCR using SYBR Green Master
417 Mix (Diagenode) on a QuantStudio 6 instrument (Themo Scientific, CA). Gene expression levels
418 were determined by using a standard curve. Each gene was normalized to the housekeeping gene
419 36B4 and was analyzed in duplicate. Primers used for real-time PCR are previously described[3,31]
420 and presented in Table 2.
421
422 **RNAScope Fluorescence in situ hybridization (FISH)**
423 mgWAT from RT or cold exposed mice (Jackson Laboratory, #000664) was fixed in 10% formalin
424 overnight, embedded with paraffin, and sectioned into unstained, 5 µm-thick sections. Sections
425 were baked at 60°C for 1 hour, deparaffinized, and baked again at 60°C for another hour prior to
426 pre-treatment. The standard pre-treatment protocol was followed for all sectioned tissues. *In situ*
427 hybridization was performed according to manufacturer's instructions using the RNAscope
428 Multiplex Fluorescent Reagent Kit v2 (#323136, Advanced Cell Diagnostics [ACD], Newark,
429 CA). Opal fluorophore reagent packs (Akoya Biosciences, Menlo Park, CA) for Opal 520
430 (FP1487A), Opal 570 (FP1488A), Opal 620 (FP1495A), and Opal 690 (FP1497A) were used at a
431 1:1000 dilution in TSA buffer (#322809, ACD). RNAscope probes from ACD were used for the
432 following targets: EPCAM (#418151), ENHO (#873251), LRG1 (#423381), LCN2 (#313971), HP
433 (#532711), WNT4 (#401101), NRG4 (#493731), KRT8 (#424528), and MFGE8 (#408778).

434 Slides were mounted with ProLong Diamond Antifade Mountant with DAPI (P36962, Life
435 Technologies, Carlsbad, CA). Fluorescent signals were captured with the 40x objective lens on a
436 laser scanning confocal microscope LSM880, (Zeiss, White Plains, NY).
437
438 **Fluorescent-activated cell sorting (FACS)**
439 Mammary gland white adipose tissue (mgWAT) from RT or cold exposed mice (Jackson
440 Laboratory, #000664) was dissected, cut, minced, and digested with collagenase D (5 mg/mL,
441 #11088882001, Roche, Germany) and dispase (2 mg/mL, #17105041, Gibco, Grand Island, NY)
442 over 40 min at 37°C with gentle shaking at 100 RPM. Enzymatic digestion was stopped with
443 DMEM/15% FBS and the cell suspension was filtered through a 100 µm nylon mesh cell strainer,
444 and centrifuged for 10 minutes at 700 x g. SVF pellet was resuspended in 1 mL Red Blood Cell
445 lysis buffer (#41027700, Roche, Germany) and incubated for 5 minutes at room temperature. Cell
446 suspension was diluted in 4 mL DPBS and filtered through a 40 µm nylon mesh cell strainer and
447 centrifuged for 10 minutes at 700 x g. Single cell suspension was blocked for 10 minutes on ice in
448 500 µL DPBS/5% BSA (blocking buffer), centrifuged for 10 min at 700 x g, resuspended in 200
449 µL of DBPS/0.5% BSA (FACS buffer) solution containing the desired antibody mix, and
450 incubated for 1 hour at 4°C in the dark with gentle rotation. Antibody-stained samples were washed
451 with 800 µL FACS buffer, centrifuged 10 minutes at 700 x g, and resuspended in FACS buffer
452 containing DAPI (at 1 ug/mL). Flow cytometry analysis was performed on a BD FACS Canto II
453 (BD Biosciences, San Jose, CA) and results analyzed on FCS Express software (DeNovo Software,
454 Pasadena, CA). Fluorescently-tagged anti-mouse antibodies (BioLegend, San Diego, CA) were
455 used to label cell surface markers for flow cytometry analysis: EPCAM-FITC (clone G8.8,
456 #118207), Sca-1-APC (Ly6, clone E13-161.7, #122512), CD49f-APC (clone GoH3, #313616).

457 For flow cytometry analysis, negative selection of CD45-expressing cells using CD45 microbeads
458 (#130052301) was performed immediately prior to the EPCAM positive selection protocol
459 described above.
460
461 **Isolation, selection, and *ex vivo* treatment of EPCAM-positive cells**
462 MACS microbeads (Miltenyi Biotec, Auburn, CA) were used for immuno-magnetic labeling
463 positive selection of EPCAM-expressing cells (anti-CD326, #130105958). Before magnetic
464 labeling, a single-cell suspension from the stromal vascular fraction of female mouse iWAT was
465 prepared in MACS buffer, i.e. PBS, pH 7.2, 0.5% bovine serum albumin (#A7030, SIGMA, St.
466 Louis, MO) and 2 mM EDTA, filtered through a MACS pre-separation 30 µm nylon mesh
467 (#130041407) to remove cell clumps. Then, for magnetic labeling of EPCAM-expressing cells, 10
468 µL of EPCAM microbeads were added per $1x10^7$ total cells in 100 uL buffer, incubated for 15
469 minutes with rotation at 4°C, washed with 1 mL buffer, centrifuged at 700 x *g* for 5 minutes,
470 resuspended in 500 µL buffer, and added to a pre-equilibrated MACS LS column (#130042401)
471 in the magnetic field of a MACS separator (#130042302). Unlabeled EPCAM-negative cells were
472 collected in the flow-through with three subsequent washes. The column was removed from the
473 magnetic field, 5 mL of MACS buffer were added to the column, and the magnetically-labeled
474 EPCAM-positive cells retained in the column were collected by flushing the cells down the column
475 with a plunger. Finally, EPCAM-negative and EPCAM-positive cell populations were centrifuged
476 at 700 x *g* for 5 minutes, resuspended in DMEM/F12 with glutamax supplemented with 15% FBS
477 and 1% pen/strep (Thermo Scientific, CA) and plated on Collagen I-coated 12-well tissue culture
478 plates (#354500, Corning, Kennebunk, ME). Media was replaced every other day during 6 days,
479 followed by cell lysis with Tryzol for phenol/chloroform RNA extraction, and RT-qPCR analysis.

480 **Adipocyte differentiation and treatments**

481 10T1/2 or SVF from the 4th inguinal (iWAT) mgWAT was isolated from 8 week old female *Lcn2*-
482 null mice, respectively. 10T1/2 cells were maintained as previously described[3]. The pre-iWAT
483 cells were maintained in Dulbecco's Modified Eagle Medium: Nutrient Mixture F-12
484 (DMEM/F12) supplemented with 1% glutamax, 10% fetal calf serum and 100 U/ml of both
485 penicillin and streptomycin (basal media). Two days after plating (day 0), when the cells reached
486 nearly 100% confluency, the cells were treated with an induction media containing basal media
487 supplemented with 4 μg/mL insulin, 0.5 mM IBMX, 1 μM dexamethasone, and 1 μM
488 rosiglitazone. After 48 h, the cells were treated with a maintenance media containing the basal
489 media supplemented with 4 μg/mL insulin, and 1 μM rosiglitazone, with a media change every 2
490 days until day 10. For qPCR, differentiated iWAT cells were treated with 1 μg/ml recombinant
491 LCN2 (Sino Biological Inc.) or differentiated 10T1/2 cells were treated with LRG1 (R&D
492 Systems) for 24 h and then treated with isoproterenol (Sigma) for 6 h after which RNA was
493 collected.

494

495 **iDISCO and Adipoclear tissue labelling and clearing**

496 **Sample collection**

497 Immediately after cold exposure mice were anaesthetized with isoflurane (3%) and perfused with
498 heparinized saline followed by 4% paraformaldefyde (PFA) (Electron Microscopy Sciences,
499 Hatfield, PA, USA). Fat pads were carefully dissected and postfixed overnight in 4% PFA at 4°C.
500 On the following day the tissue was washed 3 times in PBS before proceeding with the optical
501 clearing protocol.

502

503 **Optical clearing**

504 Whole-mount staining and clearing was performed using the Adipo-Clear protocol as previously
505 described[1]. Dissected fat pads were dehydrated at room temperature (RT) with a methanol/B1n
506 buffer (0.3 M glycine, 0.1% Triton X-100 in H_2O, pH 7) gradient (20%, 40%, 60%, 80%, 100%),
507 incubated 3 times (1h, o/n, 2h) in 100% dichloromethane (DCM) (Sigma-Aldrich, St. Louis, MO,
508 USA) to remove hydrophobic lipids, washed twice in 100% methanol, and bleached in 5%
509 H_2O_2 overnight at 4°C to reduce tissue autofluorescence. Fat pads were then rehydrated with a
510 methanol/B1n buffer gradient (80%, 60%, 40%, 20%) and then washed twice in 100% B1n buffer
511 (1h, o/n). Primary antibodies (EPCAM: 1:250; TH: 1:500) were diluted in modified PTxwH (PBS
512 with 0.5% Trixon X-100, 0.1% Tween-20, 2 µg/ml heparin, as previously described[66] and applied
513 for 6 days at 37°C. Following 5 washes with modified PTxwH over 1 day with the last wash
514 performed overnight, secondary antibodies were diluted in modified PTxwH (1:500) and samples
515 incubated for 6 days at 37°C. Samples were washed 5 times over 1 day in modified PTxwH at 37°C,
516 5 times over 1 day in PBS at RT, embedded in 1% agarose, dehydrated with a methanol gradient
517 in H_2O (12%, 50%, 75%, 100%), washed 3 times for 1 hr in 100% methanol followed by 3 times
518 for 1 hr in DCM, before being transferred to dibenzylether (DBE) (Sigma-Aldrich) to clear.

519 **Imaging**

520 Z-stacked optical sections of whole fat pads were acquired with an Ultramicroscope II (LaVision
521 BioTec, Bielefeld, Germany) at a 1.3x magnification with a 4 µm step size and dynamic focus
522 with a maximum projection filter. Samples were then imaged in glass-bottom µ-dishes (81158,
523 Ibidi, Gräfelfing, Germany) using an inverted Zeiss LSM 710 confocal microscope with a 10x
524 (NA: 0.3) objective and a step size of 5 µm.

525

526 **Image analysis**

527 Imaris versions 9.6.0-9.7.2 (Bitplane AG, Zürich, Switzerland) were used to create digital surfaces
528 covering ducts, TH+ innervation and total sample volume (1.3x light sheet images and 10x
529 confocal images) to automatically determine volumes and intensity data. Volume reconstructions
530 were performed using the surface function with local contrast background subtraction. For
531 detection of EPCAM+ ducts in 1.3x light sheet images, a smoothing factor of 5 µm was used and
532 the threshold factor was set to correspond to the largest duct diameter in each sample. For detection
533 of TH+ nerves in 1.3x light sheet images, a smoothing factor of 3 µm and a threshold factor of 80
534 µm were used. For detection of EPCAM+ ducts in 10x confocal images, a smoothing factor of
535 3.35 µm was used and a threshold factor corresponding to the diameter of the thickest duct wall in
536 each sample was used. For detection of TH+ nerves in 10x confocal images, a smoothing factor of
537 2 µm and a threshold factor of 5 µm were used. In 10x confocal images, nerve/duct interactions
538 were defined by masking the TH channel using the TH+ nerve surface to remove any background,
539 and then masking it again using the EPCAM+ duct surface. This process revealed TH+ innervation
540 overlapping with EPCAM+ staining. A new surface was created to cover this overlapping TH+
541 innervation using a smoothing factor of 2 µm and a threshold factor of 5 µm.

542 **Statistical analyses**

543 Data are shown as mean±S.E.M. Distribution was assessed by Shapiro-Wilk test. Significance was
544 determined by a two-tailed unpaired *t* test (parametric distribution) or by a Mann-Whitney test
545 (non-parametric distribution). Significance was set at an alpha level of 0.05.

546 **Mammary gland organoids culture**

547 For organoid culture, we used a previously published protocol[67]. In brief, fat pads of 8–9-week-
548 old K8rtTA/TetO-DTA[39] virgin female mice were dissected and the lymph nodes removed.

549 Tissues were briefly washed in 70% ethanol and manually chopped into 1 mm^3 pieces. The finely
550 minced tissue was transferred to a digestion mix consisting of serum-free Leibovitz's L15 medium
551 (Gibco) containing 3 mg ml^{-1} collagenase A (Sigma) and 1.5 mg ml^{-1} trypsin (Sigma). This was
552 incubated for 1 hr at 37 °C to liberate epithelial tissue fragments ('organoids'). Isolated organoids
553 were mixed with 50 µl of phenol-red-free Matrigel (BD Biosciences) and seeded in 24-well plates.
554 The basal culture medium contained phenol-red-free DMEM/F-12 with penicillin/streptomycin,
555 10 mM HEPES (Invitrogen), Glutamax (Invitrogen), N2 (Invitrogen) and B27 (Invitrogen). The
556 basal medium was supplemented with Nrg1 (100 ng ml^{-1}, R&D), Noggin (100 ng ml^{-1}, Peprotech)
557 and R-spondin 1 (100 ng ml^{-1}, R&D). Then, 500 µl supplemented basal culture medium was added
558 per well and organoids were maintained in a 37 °C humidified atmosphere under 5% CO_2. After
559 one week in culture, mammary organoids were released from the Matrigel by breaking the matrix
560 with a P1000 pipette on ice. After 2–3 passages of washing and centrifugation at 1,500 rpm (140g)
561 for 5 min at 4 °C, mammary cells were resuspended in Matrigel, seeded in 24-well plates and
562 exposed to the previously described culture conditions. Organoids were treated either with 10 µg
563 ml^{-1} of DOX to promote luminal cell ablation or with 10µM of isoproterenol (Sigma) for 6 hr.
564 After 6 hr treatment, organoids were collected from Matrigel as mentioned before to perform
565 further analysis.

566 **RNA extraction and quantitative real-time PCR in organoid samples**

567 To perform RNA extraction, isolated organoids were collected into kit lysis buffer. RNA was
568 extracted with Qiagen RNeasy Micro Kit. After nanodrop RNA quantification and analysis of
569 RNA integrity, purified RNA was used to synthesize the first-strand cDNA in a 30 µl final volume,
570 using Superscript II (Invitrogen) and random hexamers (Roche). Genomic contamination was
571 detected by performing the same procedure without reverse transcriptase. Quantitative PCR

572 analyses were performed with 1 ng of cDNA as template, using FastStart Essential DNA green
573 master (Roche) and a Light Cycler 96 (Roche) for real-time PCR system. Relative quantitative
574 RNA was normalized using the housekeeping gene Gapdh. Analysis of the results was performed
575 using Light Cycler 96 software (Roche) and relative quantification was performed using the ddCt
576 method using Gapdh as a reference.
577

578 **Immunofluorescence in organoid samples**

579 For immunofluorescence, collected organoids were pre-fixed in 4% PFA for 30 min at RT. Pre-
580 fixed organoids were washed in 2%FBS-PBS, embedded in OCT and kept at -80°C. Sections of 4
581 µm were cut using a HM560 Microm cryostat (Mikron Instruments). Tissue sections were
582 incubated in blocking buffer (BSA 1%, HS 5%, Triton-X 0.2% in PBS) for 1 hr at RT. The different
583 primary antibodies were incubated overnight at 4 °C. Sections were then rinsed in PBS and
584 incubated with the corresponding secondary antibodies diluted at 1:400 in blocking buffer for 1 hr
585 at RT. The following primary antibodies were used: rat anti-K8 (1:1,000, Troma-I, Developmental
586 Studies Hybridoma Bank, University of Iowa), rabbit anti-EPCAM (1:1,000, ab71916, Abcam),
587 goat anti-Lcn2 (1:50, AF1857, R&D). The following secondary antibodies, diluted 1:400, were
588 used: anti-goat (A11055) conjugated to Alexa Fluor 488 (Invitrogen), anti-rat (712-295-155)
589 rhodamine Red-X and anti-rabbit (711-605-152) Cy5 (Jackson ImmunoResearch). Nuclei were
590 stained with Hoechst solution (1:2,000) and slides were mounted in DAKO mounting medium
591 supplemented with 2.5% DABCO (Sigma).
592

593 **Conflict of Interests (COI)**

594 AJB is a co-founder and consultant to Personalis and NuMedii; consultant to Samsung, Mango
595 Tree Corporation, and in the recent past, 10 × Genomics, Helix, Pathway Genomics, and Verinata

596 (Illumina); has served on paid advisory panels or boards for Geisinger Health, Regenstrief
597 Institute, Gerson Lehman Group, AlphaSights, Covance, Novartis, Genentech, and Merck, and
598 Roche; is a shareholder in Personalis and NuMedii; is a minor shareholder in Apple, Facebook,
599 Alphabet (Google), Microsoft, Amazon, Snap, 10 × Genomics, Illumina, CVS, Nuna Health,
600 Assay Depot, Vet24seven, Regeneron, Sanofi, Royalty Pharma, AstraZeneca, Moderna, Biogen,
601 Paraxel, and Sutro, and several other non-health related companies and mutual funds; and has
602 received honoraria and travel reimbursement for invited talks from Johnson and Johnson, Roche,
603 Genentech, Pfizer, Merck, Lilly, Takeda, Varian, Mars, Siemens, Optum, Abbott, Celgene,
604 AstraZeneca, AbbVie, Westat, and many academic institutions, medical or disease specific
605 foundations and associations, and health systems. AJB receives royalty payments through Stanford
606 University, for several patents and other disclosures licensed to NuMedii and Personalis. AJB's
607 research has been funded by NIH, Northrup Grumman (as the prime on an NIH contract),
608 Genentech, Johnson and Johnson, FDA, Robert Wood Johnson Foundation, Leon Lowenstein
609 Foundation, Intervalien Foundation, Priscilla Chan and Mark Zuckerberg, the Barbara and Gerson
610 Bakar Foundation, and in the recent past, the March of Dimes, Juvenile Diabetes Research
611 Foundation, California Governor's Office of Planning and Research, California Institute for
612 Regenerative Medicine, L'Oreal, and Progenity.
613 SAS is a named inventor of the intellectual property, "Compositions and Methods to Modulate
614 Cell Activity", a co-founder of and has equity in the private company Redpin Therapeutics.
615 The rest of the authors declare no COIs.

616 **Acknowledgements**

617 A.A is supported by senior postdoctoral fellowship from the Charles H. Revson Foundation (grant
618 no. 18-25), a fellowship from Sweden-America Foundation (Ernst O Eks fond), and a postdoctoral

619 scholarship from the Swedish Society for Medical Research (SSMF). S.A.S is supported by
620 American Diabetes Association Pathway to Stop Diabetes Grant ADA #1-17-ACE-31 NIH
621 (R01NS097184, OT2OD024912, and R01DK124461) Department of Defense (W81XWH-20-1-
622 0345, W81XWH-20-1-0156). A.J.L is supported by NIH U01 AG070959 and U54 DK120342.
623 P.R is supported by R00DK114571, NIDDK-supported Einstein-Sinai Diabetes Research Center
624 (DRC) Pilot & Feasibility Award, and Diabetes Research and Education Foundation (DREF) Grant
625 # 501 (PR). The funders had no role in study design, data collection and interpretation, or the
626 decision to submit the work for publication.

627

628 **Contributions**

629 D.A. performed all the scRNA-seq data analysis under the supervision of X.Y. L.C.S. performed
630 most of the biological experiments under the supervision of P.R. A.A. performed iDISCO and data
631 analysis under the supervision of S.A.S. K.C.K performed LCN2 related animal experiments under
632 the supervision of A.J.L. A.C.S performed organoid experiments under the supervision of C.B.
633 S.P. performed RNAscope and EPCAM cells isolation experiments under supervision of L.C.S
634 and P.R. S.S. performed indirect calorimetry and body composition studies under the supervision
635 of P.R.. I.S.A, G.D., and I.C., prepared single cell suspensions of mgWAT SVFs under the
636 supervision of P.R. and X.Y.. P.R. conceived the project and wrote the manuscript with help from
637 A.J.B., C.B., S.A.S, A.J.L., and X.Y.

638

639

640 **REFERENCES**

641 1 Chi, J. *et al.* Three-Dimensional Adipose Tissue Imaging Reveals Regional Variation in
642 Beige Fat Biogenesis and PRDM16-Dependent Sympathetic Neurite Density. *Cell Metab*
643 **27**, 226-236 e223, doi:10.1016/j.cmet.2017.12.011 (2018).
644 2 Zhang, F. *et al.* An Adipose Tissue Atlas: An Image-Guided Identification of Human-like
645 BAT and Beige Depots in Rodents. *Cell Metab* **27**, 252-262.e253,
646 doi:10.1016/j.cmet.2017.12.004 (2018).
647 3 Rajbhandari, P. *et al.* IL-10 Signaling Remodels Adipose Chromatin Architecture to Limit
648 Thermogenesis and Energy Expenditure. *Cell* **172**, 218-233 e217,
649 doi:10.1016/j.cell.2017.11.019 (2018).
650 4 Knights, A. J., Wu, J. & Tseng, Y.-H. The Heating Microenvironment: Intercellular Cross
651 Talk Within Thermogenic Adipose Tissue. *Diabetes* **69**, 1599, doi:10.2337/db20-0303
652 (2020).
653 5 Li, J. *et al.* Neurotensin is an anti-thermogenic peptide produced by lymphatic endothelial
654 cells. *Cell Metab* **33**, 1449-1465.e1446, doi:10.1016/j.cmet.2021.04.019 (2021).
655 6 Hu, B. *et al.* γδ T cells and adipocyte IL-17RC control fat innervation and thermogenesis.
656 *Nature* **578**, 610-614, doi:10.1038/s41586-020-2028-z (2020).
657 7 Wang, Q. *et al.* IL-27 signalling promotes adipocyte thermogenesis and energy
658 expenditure. *Nature*, doi:10.1038/s41586-021-04127-5 (2021).
659 8 Gjorevski, N. & Nelson, C. M. Integrated morphodynamic signalling of the mammary
660 gland. *Nat Rev Mol Cell Biol* **12**, 581-593, doi:10.1038/nrm3168 (2011).
661 9 McNally, S. & Martin, F. Molecular regulators of pubertal mammary gland development.
662 *Ann Med* **43**, 212-234, doi:10.3109/07853890.2011.554425 (2011).
663 10 Inman, J. L., Robertson, C., Mott, J. D. & Bissell, M. J. Mammary gland development: cell
664 fate specification, stem cells and the microenvironment. *Development* **142**, 1028-1042,
665 doi:10.1242/dev.087643 (2015).
666 11 Wang, Q. A. & Scherer, P. E. Remodeling of Murine Mammary Adipose Tissue during
667 Pregnancy, Lactation, and Involution. *J Mammary Gland Biol Neoplasia* **24**, 207-212,
668 doi:10.1007/s10911-019-09434-2 (2019).
669 12 Landskroner-Eiger, S., Park, J., Israel, D., Pollard, J. W. & Scherer, P. E. Morphogenesis
670 of the developing mammary gland: stage-dependent impact of adipocytes. *Dev Biol* **344**,
671 968-978, doi:10.1016/j.ydbio.2010.06.019 (2010).
672 13 Wang, Q. A. *et al.* Reversible De-differentiation of Mature White Adipocytes into
673 Preadipocyte-like Precursors during Lactation. *Cell Metab* **28**, 282-288 e283,
674 doi:10.1016/j.cmet.2018.05.022 (2018).
675 14 Butler, A., Hoffman, P., Smibert, P., Papalexi, E. & Satija, R. Integrating single-cell
676 transcriptomic data across different conditions, technologies, and species. *Nat Biotechnol*
677 **36**, 411-420, doi:10.1038/nbt.4096 (2018).
678 15 Arneson, D. *et al.* Single cell molecular alterations reveal target cells and pathways of
679 concussive brain injury. *Nat Commun* **9**, 3894, doi:10.1038/s41467-018-06222-0 (2018).
680 16 Bach, K. *et al.* Differentiation dynamics of mammary epithelial cells revealed by single-
681 cell RNA sequencing. *Nat Commun* **8**, 2128, doi:10.1038/s41467-017-02001-5 (2017).
682 17 Tabula Muris, C. *et al.* Single-cell transcriptomics of 20 mouse organs creates a Tabula
683 Muris. *Nature* **562**, 367-372, doi:10.1038/s41586-018-0590-4 (2018).

18 Tabula Muris, C. A single-cell transcriptomic atlas characterizes ageing tissues in the mouse. *Nature* **583**, 590-595, doi:10.1038/s41586-020-2496-1 (2020).

19 Li CM, S. H., Tsiobikas C, Selfors L, Chen H, Gray GK, Oren Y, Pinello L, Regev A, Brugge JS. Aging-associated alterations in the mammary gland revealed by single-cell RNA sequencing. *bioRxiv* (2019).

20 Li, C. M.-C. *et al.* Aging-Associated Alterations in Mammary Epithelia and Stroma Revealed by Single-Cell RNA Sequencing. *Cell Reports* **33**, 108566, doi:https://doi.org/10.1016/j.celrep.2020.108566 (2020).

21 Aryal, B. *et al.* Absence of ANGPTL4 in adipose tissue improves glucose tolerance and attenuates atherogenesis. *JCI Insight* **3**, doi:10.1172/jci.insight.97918 (2018).

22 De Keyser, J., De Backer, J. P., Ebinger, G. & Vauquelin, G. Regional distribution of the dopamine D2 receptors in the mesotelencephalic dopamine neuron system of human brain. *J Neurol Sci* **71**, 119-127, doi:10.1016/0022-510x(85)90041-3 (1985).

23 Arner, E. *et al.* Ceruloplasmin is a novel adipokine which is overexpressed in adipose tissue of obese subjects and in obesity-associated cancer cells. *PLoS One* **9**, e80274, doi:10.1371/journal.pone.0080274 (2014).

24 Chella Krishnan, K. *et al.* Sex-specific metabolic functions of adipose Lipocalin-2. *Mol Metab* **30**, 30-47, doi:10.1016/j.molmet.2019.09.009 (2019).

25 Sun, W. Y. *et al.* Lipocalin-2 derived from adipose tissue mediates aldosterone-induced renal injury. *JCI Insight* **3**, doi:10.1172/jci.insight.120196 (2018).

26 Deis, J. A. *et al.* Adipose Lipocalin 2 overexpression protects against age-related decline in thermogenic function of adipose tissue and metabolic deterioration. *Mol Metab* **24**, 18-29, doi:10.1016/j.molmet.2019.03.007 (2019).

27 Ishii, A. *et al.* Obesity-promoting and anti-thermogenic effects of neutrophil gelatinase-associated lipocalin in mice. *Sci Rep* **7**, 15501, doi:10.1038/s41598-017-15825-4 (2017).

28 Wang, G. X. *et al.* The brown fat-enriched secreted factor Nrg4 preserves metabolic homeostasis through attenuation of hepatic lipogenesis. *Nat Med* **20**, 1436-1443, doi:10.1038/nm.3713 (2014).

29 Maffei, M., Barone, I., Scabia, G. & Santini, F. The Multifaceted Haptoglobin in the Context of Adipose Tissue and Metabolism. *Endocr Rev* **37**, 403-416, doi:10.1210/er.2016-1009 (2016).

30 Kumar, K. G. *et al.* Identification of adropin as a secreted factor linking dietary macronutrient intake with energy homeostasis and lipid metabolism. *Cell Metab* **8**, 468-481, doi:10.1016/j.cmet.2008.10.011 (2008).

31 Rajbhandari, P. *et al.* Single cell analysis reveals immune cell-adipocyte crosstalk regulating the transcription of thermogenic adipocytes. *Elife* **8**, doi:10.7554/eLife.49501 (2019).

32 Gargiulo, L. *et al.* A Novel Effect of beta-Adrenergic Receptor on Mammary Branching Morphogenesis and its Possible Implications in Breast Cancer. *J Mammary Gland Biol Neoplasia* **22**, 43-57, doi:10.1007/s10911-017-9371-1 (2017).

33 Marchetti, B. *et al.* Beta-adrenergic receptors in the rat mammary gland during pregnancy and lactation: characterization, distribution, and coupling to adenylate cyclase. *Endocrinology* **126**, 565-574, doi:10.1210/endo-126-1-565 (1990).

34 Nedvetsky, P. I., Kwon, S. H., Debnath, J. & Mostov, K. E. Cyclic AMP regulates formation of mammary epithelial acini in vitro. *Mol Biol Cell* **23**, 2973-2981, doi:10.1091/mbc.E12-02-0078 (2012).

35 Gargiulo, L. *et al.* A Novel Effect of β-Adrenergic Receptor on Mammary Branching Morphogenesis and its Possible Implications in Breast Cancer. *J Mammary Gland Biol Neoplasia* **22**, 43-57, doi:10.1007/s10911-017-9371-1 (2017).

36 Feng, Y., Manka, D. R., Wagner, K.-U. & Khan, S. A. Estrogen receptor0± expression in the mammary epithelium is required for ductal and alveolar morphogenesis in mice. *Proceedings of the National Academy of Sciences* **104**, 14718 - 14723 (2007).

37 Lawson, D. A., Werb, Z., Zong, Y. & Goldstein, A. S. The Cleared Mammary Fat Pad Transplantation Assay for Mammary Epithelial Organogenesis. *Cold Spring Harb Protoc* **2015**, pdb.prot078071, doi:10.1101/pdb.prot078071 (2015).

38 Chi, J. *et al.* Three-Dimensional Adipose Tissue Imaging Reveals Regional Variation in Beige Fat Biogenesis and PRDM16-Dependent Sympathetic Neurite Density. *Cell Metab* **27**, 226-236.e223, doi:10.1016/j.cmet.2017.12.011 (2018).

39 Centonze, A. *et al.* Heterotypic cell-cell communication regulates glandular stem cell multipotency. *Nature* **584**, 608-613, doi:10.1038/s41586-020-2632-y (2020).

40 Bauters, D., Van Hul, M. & Lijnen, H. R. Macrophage elastase (MMP-12) in expanding murine adipose tissue. *Biochim Biophys Acta* **1830**, 2954-2959, doi:10.1016/j.bbagen.2012.12.024 (2013).

41 Lee, J. T. *et al.* Macrophage metalloelastase (MMP12) regulates adipose tissue expansion, insulin sensitivity, and expression of inducible nitric oxide synthase. *Endocrinology* **155**, 3409-3420, doi:10.1210/en.2014-1037 (2014).

42 Shao, M. *et al.* Zfp423 Maintains White Adipocyte Identity through Suppression of the Beige Cell Thermogenic Gene Program. *Cell Metab* **23**, 1167-1184, doi:10.1016/j.cmet.2016.04.023 (2016).

43 Gavalda-Navarro, A. *et al.* Lipopolysaccharide-binding protein is a negative regulator of adipose tissue browning in mice and humans. *Diabetologia* **59**, 2208-2218, doi:10.1007/s00125-016-4028-y (2016).

44 Sun, W. *et al.* snRNA-seq reveals a subpopulation of adipocytes that regulates thermogenesis. *Nature* **587**, 98-102, doi:10.1038/s41586-020-2856-x (2020).

45 Kiefer, F. W. *et al.* Retinaldehyde dehydrogenase 1 regulates a thermogenic program in white adipose tissue. *Nat Med* **18**, 918-925, doi:10.1038/nm.2757 (2012).

46 Mina, A. I. *et al.* CalR: A Web-Based Analysis Tool for Indirect Calorimetry Experiments. *Cell Metab* **28**, 656-666 e651, doi:10.1016/j.cmet.2018.06.019 (2018).

47 Dobin, A. *et al.* STAR: ultrafast universal RNA-seq aligner. *Bioinformatics* **29**, 15-21, doi:10.1093/bioinformatics/bts635 (2013).

48 Kim, D., Langmead, B. & Salzberg, S. L. HISAT: a fast spliced aligner with low memory requirements. *Nat Methods* **12**, 357-360, doi:10.1038/nmeth.3317 (2015).

49 Love, M. I., Anders, S., Kim, V. & Huber, W. RNA-Seq workflow: gene-level exploratory analysis and differential expression. *F1000Res* **4**, 1070, doi:10.12688/f1000research.7035.1 (2015).

50 Hafemeister, C. & Satija, R. Normalization and variance stabilization of single-cell RNA-seq data using regularized negative binomial regression. *Genome Biol* **20**, 296, doi:10.1186/s13059-019-1874-1 (2019).

51 Butler, A., Hoffman, P., Smibert, P., Papalexi, E. & Satija, R. Integrating single-cell transcriptomic data across different conditions, technologies, and species. *Nature Biotechnology* **36**, 411-420, doi:10.1038/nbt.4096 (2018).

52 Stuart, T. *et al.* Comprehensive Integration of Single-Cell Data. *Cell* **177**, 1888-1902.e1821, doi:10.1016/j.cell.2019.05.031 (2019).
53 McInnes, L., Healy, J. & Melville, J. UMAP: Uniform Manifold Approximation and Projection for Dimension Reduction. *arXiv* (2018).
54 van der Maaten, L. & Hinton, G. Visualizing Data using t-SNE. *J Mach Learn Res*, 2579-2605 (2008).
55 Blondel, V. D., Guillaume, J.-L., Lambiotte, R. & Lefebvre, E. Fast unfolding of communities in large networks. *J. Stat. Mech.* **2008**, P10008, doi:10.1088/1742-5468/2008/10/P10008 (2008).
56 Broad Institute. *Study: Mouse Adipose Stromal Vascular Fraction*, <https://singlecell.broadinstitute.org/single_cell/study/SCP708/mouse-adipose-stromal-vascular-fraction#study-summary> (
57 Bach, K. *et al.* Differentiation dynamics of mammary epithelial cells revealed by single-cell RNA sequencing. *Nature Communications* **8**, 2128, doi:10.1038/s41467-017-02001-5 (2017).
58 Guo, G. MCA DGE Data. *Figshare*, doi:10.6084/m9.figshare.5435866.v8 (2020).
59 Han, X. *et al.* Mapping the Mouse Cell Atlas by Microwell-Seq. *Cell* **172**, 1091-1107.e1017, doi:10.1016/j.cell.2018.02.001 (2018).
60 Tabula Muris: Transcriptomic characterization of 20 organs and tissues from Mus musculus at single cell resolution.
61 Tabula Muris Senis.
62 Kanehisa, M. & Goto, S. KEGG: Kyoto Encyclopedia of Genes and Genomes. *Nucleic Acids Res* **28**, 27-30, doi:10.1093/nar/28.1.27 (2000).
63 Jassal, B. *et al.* The Reactome Pathway Knowledgebase. *Nucleic Acids Res* **48**, D498-D503, doi:10.1093/nar/gkz1031 (2020).
64 Nishimura, D. BioCarta. *Biotech Software & Internet Report* **2**, 117-120, doi:10.1089/152791601750294344 (2001).
65 Ashburner, M. *et al.* Gene Ontology: tool for the unification of biology. *Nat Genet* **25**, 25-29, doi:10.1038/75556 (2000).
66 Alvarsson, A. *et al.* Optical Clearing and 3D Analysis Optimized for Mouse and Human Pancreata. *Bio Protoc* **11**, e4103, doi:10.21769/BioProtoc.4103 (2021).
67 Jardé, T. *et al.* Wnt and Neuregulin1/ErbB signalling extends 3D culture of hormone responsive mammary organoids. *Nature Communications* **7**, 13207, doi:10.1038/ncomms13207 (2016).

Main Figure 1

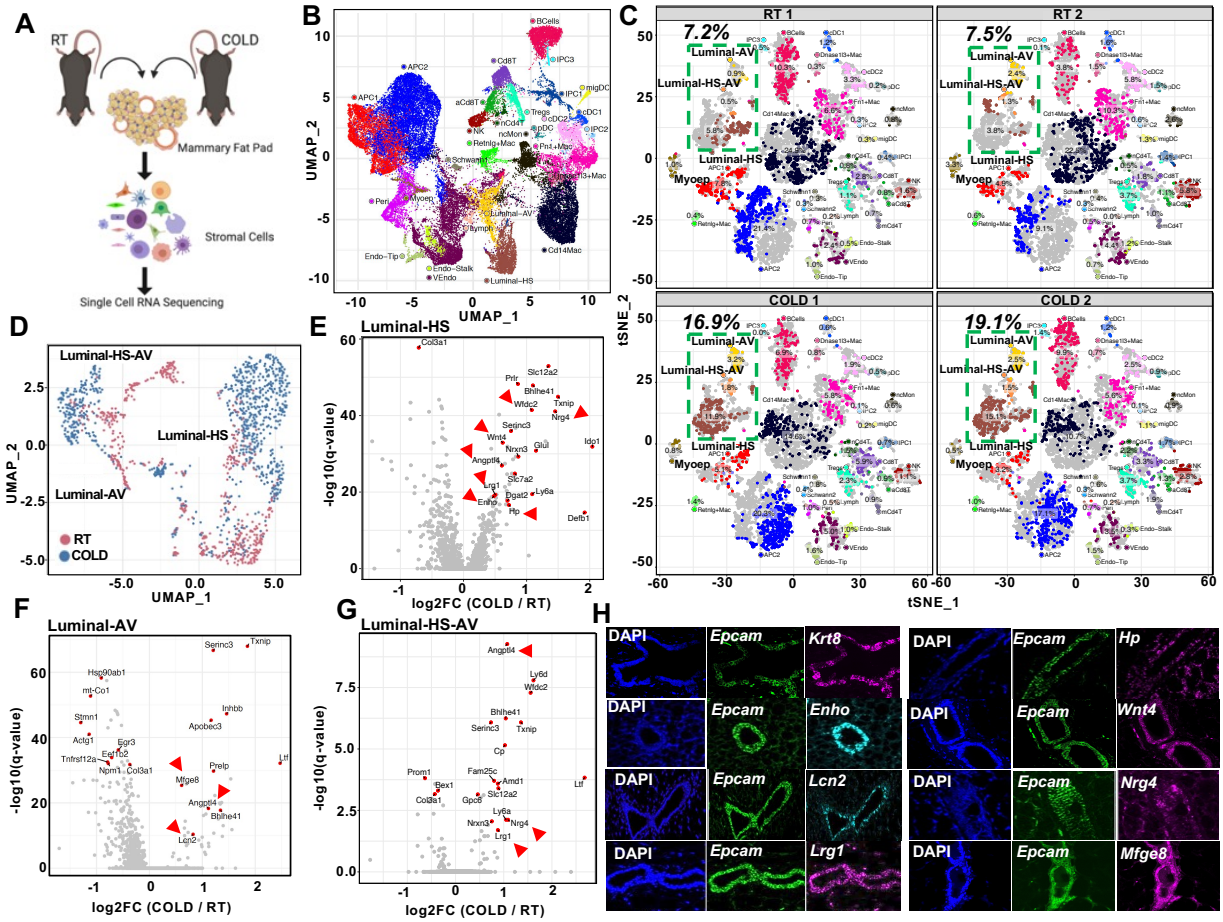

Figure 1. Deconstruction of mgWAT shows cold-induced remodeling of mammary epithelium

(A) Cartoon depiction of the scRNA-seq workflow showing isolation of stromal vascular fraction (stromal cells) from mammary fat pad (mgWAT) of 10-week-old 24 h RT or COLD exposed female mice. **(B)** UMAP plots of integrated single cell data from this study and 8 external datasets (see Methods). Each point represents a single cell and clusters are colored by cell type**. (C)** t-SNE plot of single cells from mammary gland and surrounding SVF colored by cell type and separated by sample. Relative fractions of each cell type in each sample are indicated on each cluster. Room temperature (RT) samples are on the top row and 4°C (COLD) are on the bottom row. **(D)** UMAP

826 plot of luminal epithelial cell types from RT or cold mgWATs. **(E-G)** Differentially expressed
827 genes between COLD treated mice and RT animals across Luminal-HS (E), Luminal-AV (F), and
828 Luminal-HS-AV (G). Select significant DEGs (adjusted p-value < 0.05) are highlighted with the
829 average log fold change between 4 degree and RT indicated on the y-axis. Genes indicated by red
830 arrows encode for secreted factors. **(H)** RNAScope FISH (see Materials and methods) of indicated
831 probes from mgWAT of 24 hr cold exposed mice.
832
833 Abbreviations: APC, adipose precursor cells; IPC, immune precursor cells; Mac, macrophages;
834 ncMon, non-classical monocytes; cDC, conventional dendritic cells; migDC, migratory dendritic
835 cells; pDC, plasmacytoid dendritic cells; Tregs, regulatory T cells; mCd4T, memory Cd4 T cells;
836 nCd4T, naïve Cd4 T cells; aCd8T, activated Cd8 T cells; Myoep, myoepithelial cells; VEndo,
837 vascular endothelial cells; Endo-Tip, endothelial tip cells; Endo-Stalk, endothelial stalk cells;
838 Lymph, lymphatic endothelial cells; Peri, pericytes; Luminal-HS, hormone-sensing luminal cells;
839 Luminal-AV, secretory alveolar luminal cells; Luminal-HS-AV.
840
841
842
843
844
845
846
847
848

849

850 **Main Figure 2**

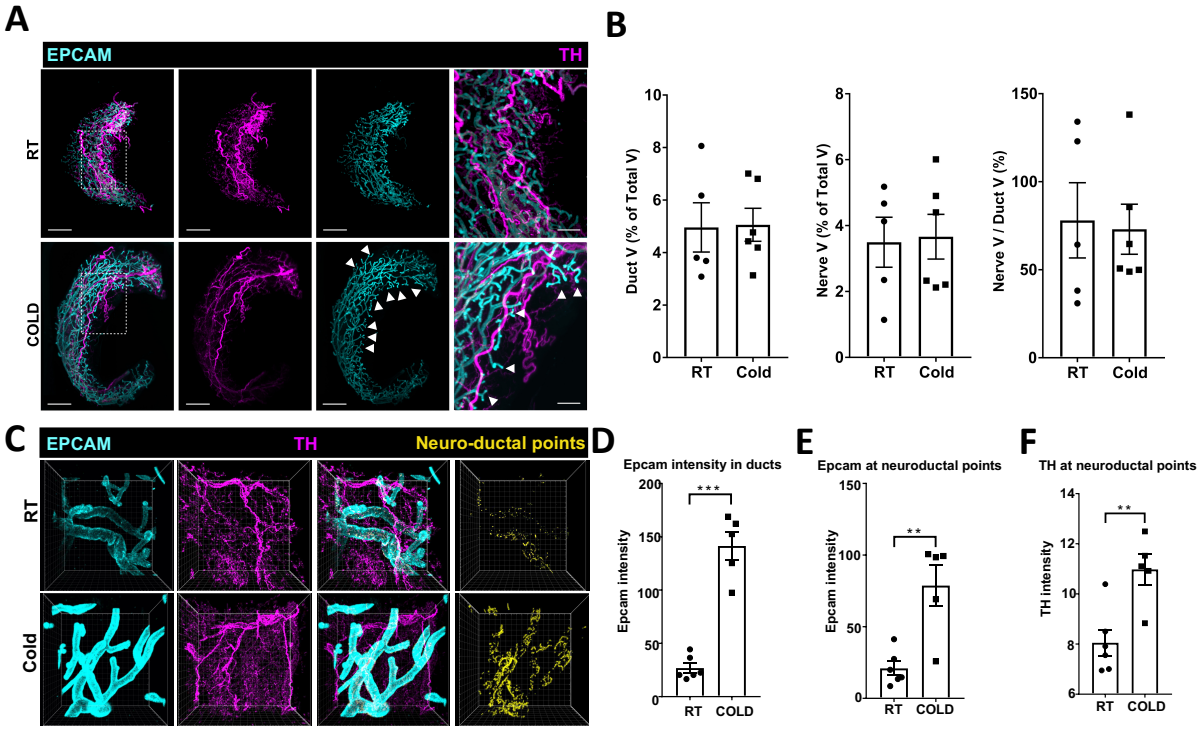

851

852

853 **Figure 2. SNS fibers directly innervate mammary ductal epithelium**

854 **(A)** Light sheet microscopy fluorescence (LSFM) images of mgWAT isolated from female mice
855 exposed to RT or COLD for 24 hr and stained with TH antibody (SNS fibers) and EPCAM
856 antibody (ductal cells). Representative mgWAT images from 5-6 mice per condition. White arrows
857 show terminal ductal bifurcations under COLD condition **(B)** Quantification of LSFM images for
858 ductal volume (Duct V) and nerve volume (Nerve V) as a percentage of total volume (Total V),
859 and ratio of Nerve V and Duct V in RT or COLD mgWATs N=5-6 per condition. **(C)** Confocal
860 images of mgWAT isolated from female mice exposed to RT or COLD (24 hr) and stained for
861 EPCAM and TH antibodies. Merged stainings of EPCAM and TH represent neuroductal points.
862 Representative image of 5-6 mice per condition.

(D-F) Quantification of EPCAM intensity in ducts (D), EPCAM intensity at neuroductal points (E), and TH intensity at neuroductal points (F). N=5-6 per condition. **, $p<0.01$; ***, $p<0.001$.

886 **Main Figure 3**

887

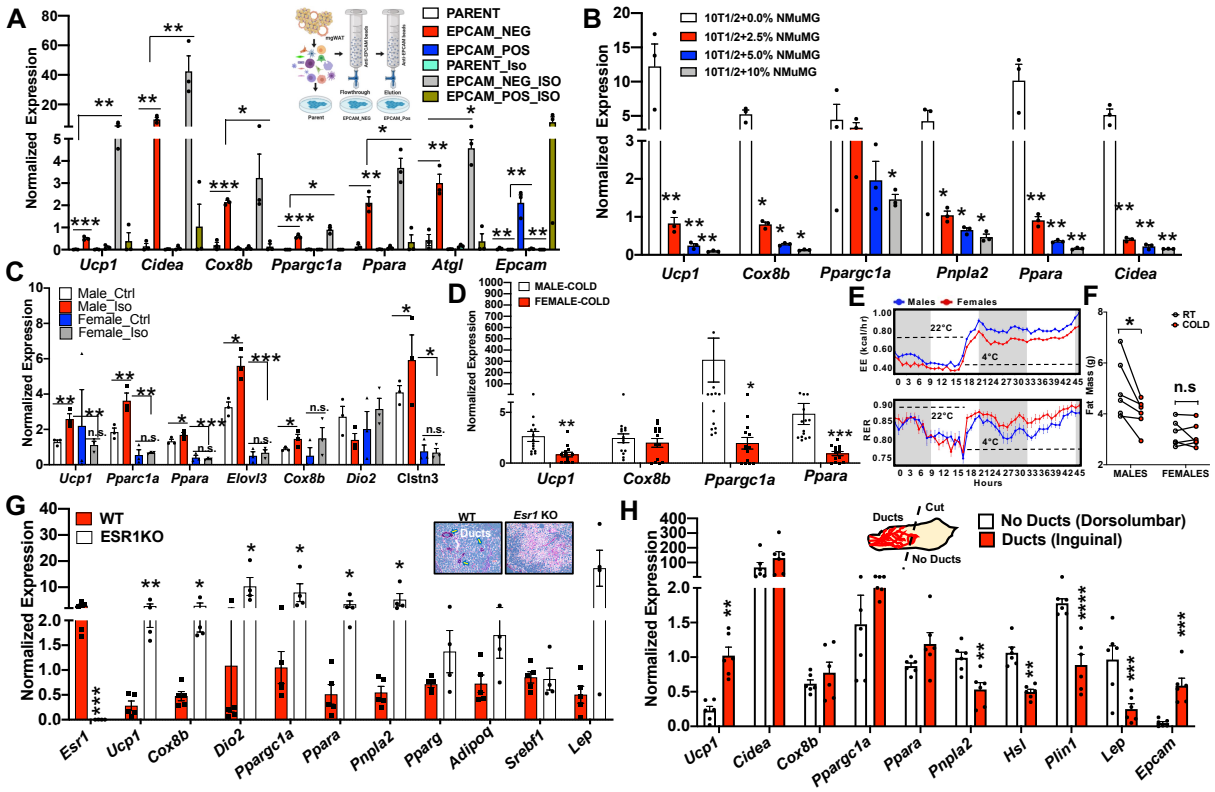

888

889 **Figure 3. Mammary ductal cells directly inhibit adipocyte thermogenesis.**

890 **A)** Real-time qPCR of indicated genes from beige differentiation of primary mgWAT SVF
891 (Parent), EPCAM-ve (EPCAM-NEG), and EPCAM+ (EPCAM-POS) cells treated with and
892 without 10 μM isoproterenol (ISO) for 24 hr. Results are from three independent experiments. *,
893 p<0.05**;** **, p<0.01; ***, p<0.001. Inset represent a cartoon depiction of selecting and plating
894 EPCAM+ cells from SVFs derived from mgWATs. **B)** Real-time qPCR of indicated genes from
895 beige differentiated and Iso treated 10T1/2 and 2.5-10% NMuMG mixture cells. Results are from
896 three independent experiments. *, p<0.05**;** **, p<0.01. **C)** Real-time qPCR of indicated genes from
897 beige differentiated SVFs isolated from male and female iWATs treated with and without Iso.
898 Results are from three independent experiments. *, p<0.05**,** **, p<0.01; ***, p<0.001**. D)** Real-

time qPCR of indicated genes from 24 h cold exposed male and female iWATs. N=13,13 *, $p<0.05$, **, $p<0.01$; ***, $p<0.001$. **E)** Energy expenditure (kcal/hr) and respiratory exchange ratio (RER) of male and female mice exposed to 22°C (21 hr) and 4°C (24 hr) analyzed in Sable Promethion metabolic chambers (12 hr light/dark cycle, 45 hr total duration, white bar represent light cycle and grey bar represent night cycle). N=6,6. **F)** Fat mass of mice from (E) at RT (22°C) and COLD (4°C). N=6,6. *, $p<0.05$; n.s, not significant. **G)** Real-time qPCR of indicated genes from 24 hr cold exposed WT and *Esr1* KO mgWATs. Inset picture shows histological section of mgWATs from WT and *Esr1* KO mice. Arrows are pointing towards ducts in WT. N=5,5 *, $p<0.05$, **, $p<0.01$. **H)** Real-time qPCR of indicated genes from dorsolumbar or inguinal parts of cold-exposed 5-week-old mice. Inset picture shows cartoon depiction of ducts (inguinal) and no ducts (dorsolumbar). Dotted line represents cut site to separate inguinal and dorsolumbar regions of mgWAT. N=6,6. *, $p<0.05$, **, $p<0.01$; ***, $p<0.001$

922 **Main Figure 4**

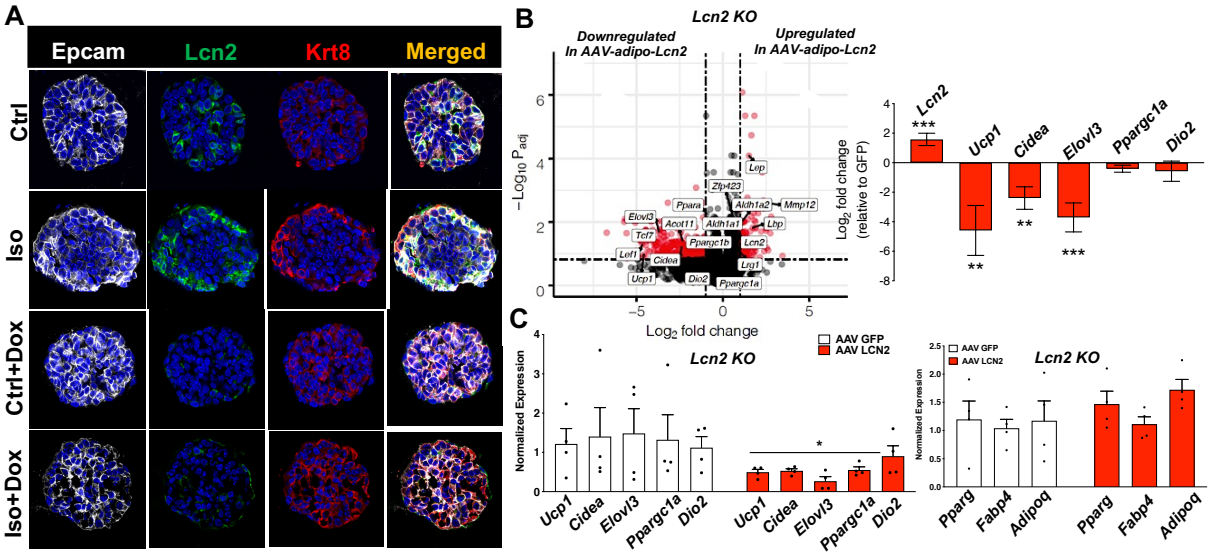

923

924 **Figure 4. LCN2 preserves mgWAT adiposity.**

925 **A)** Confocal images of immunostaining of indicated antibodies in the organoids derived from
926 K8rtTA-DTA mice (see Methods) treated with and without Iso and Doxycycline (Dox).
927 Representative images from 3 organoid experiments. **B)** Volcano plot of DEGs from the mgWAT
928 of *Lcn2* KO mice treated with adipose-specific AAV-LCN2 or AAV-GFP and represented as a
929 fold change of LCN2/GFP ratio as a function of p-value. Genes labelled are either induced (+) or
930 repressed (-) by Lcn2. **, $p<0.01$; ***, $p<0.001$. N=4,4. **C)** Real-time qPCR of indicated genes
931 from the mgWATs of LCN2KO or WT mice treated with AAV-LCN2 or AAV-GFP. N=4,4. *,
932 $p<0.05$

933

934

935

936

Extended Data Figure 1

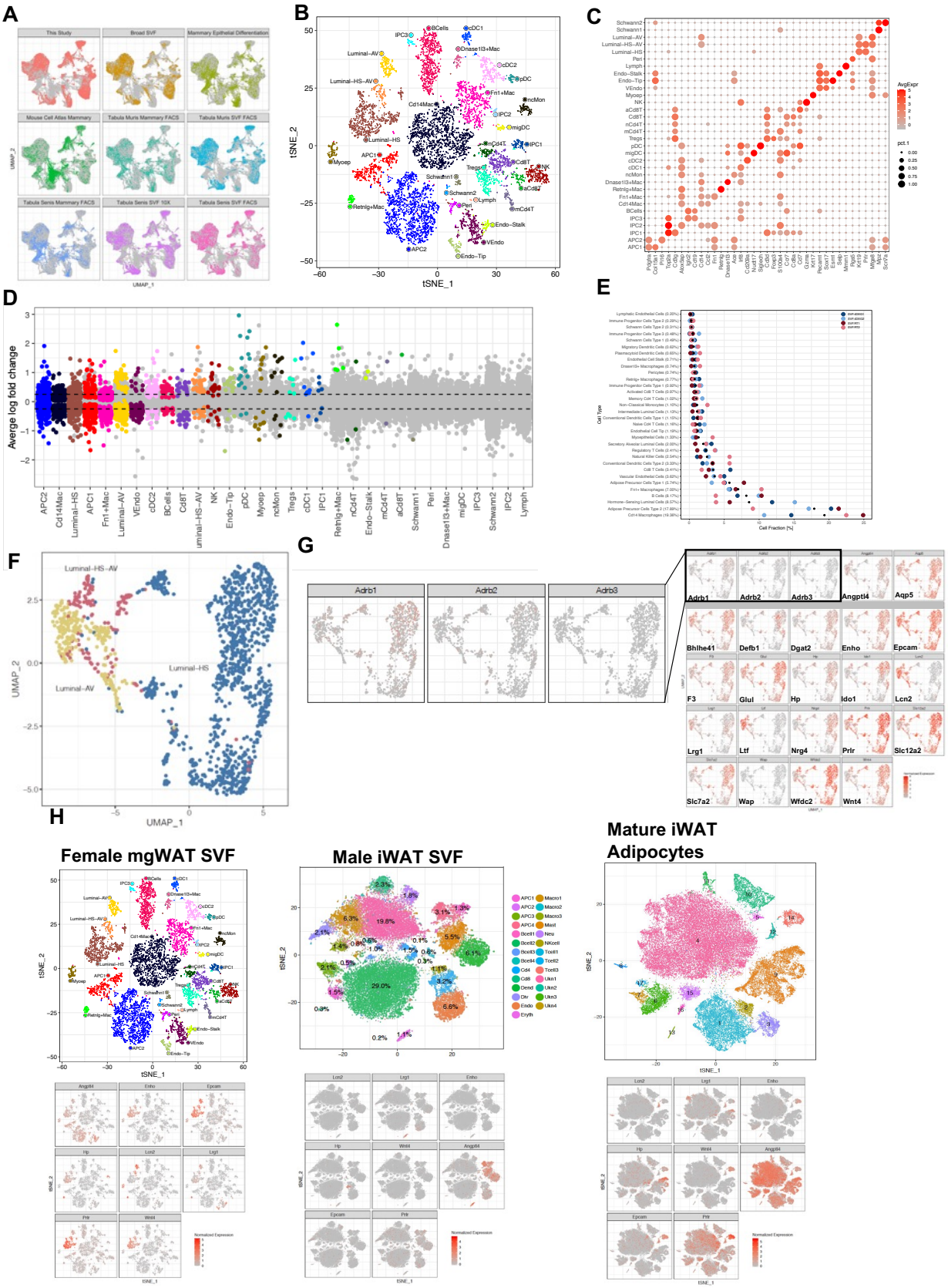

938 **Figure 1. Cold-associated increase in cell percentages of luminal epithelium subtypes.**
939 **A)** UMAP plots of integrated single cell data from this study and 8 external datasets (see Methods
940 and Table 1). Each point represents a single cell and are colored by dataset. **B)** t-SNE plot of single
941 cells from mammary gland and surrounding SVF from this study colored by cell type. Cell types
942 were identified based on expression of canonical marker genes. **C)** Expression of known canonical
943 markers for cell types in the SVF and mammary gland. Color corresponds to average expression
944 level and size corresponds to percentage of cells which express the gene within the cluster. **D)**
945 Differentially expressed genes between COLD (24 hr) treated mice and RT animals across all cell
946 types. Significant DEGs (adjusted p-value < 0.05) are highlighted with the average log fold change
947 between 4 degree and RT indicated on the y-axis. Cell types are ordered on the x-axis based on
948 the number of significant DEGs. **E)** Relative fractions of cell types within each sample. Black dots
949 indicate average relative fractions across all samples. **F)** Aggregated UMAP plot of subclustering
950 of luminal single cells from RT and cold-exposed mice. **G)** UMAP plots of normalized gene
951 expression levels for genes of interest in luminal cells. **H)** tSNE plots of cell type clusters and
952 normalized gene expression levels for genes of interest across multiple datasets including: female
953 mgWAT SVFs, male iWAT SVFs and mature mgWAT adipocytes.
954
955
956
957
958
959
960

961 **Extended Data Figure 2**

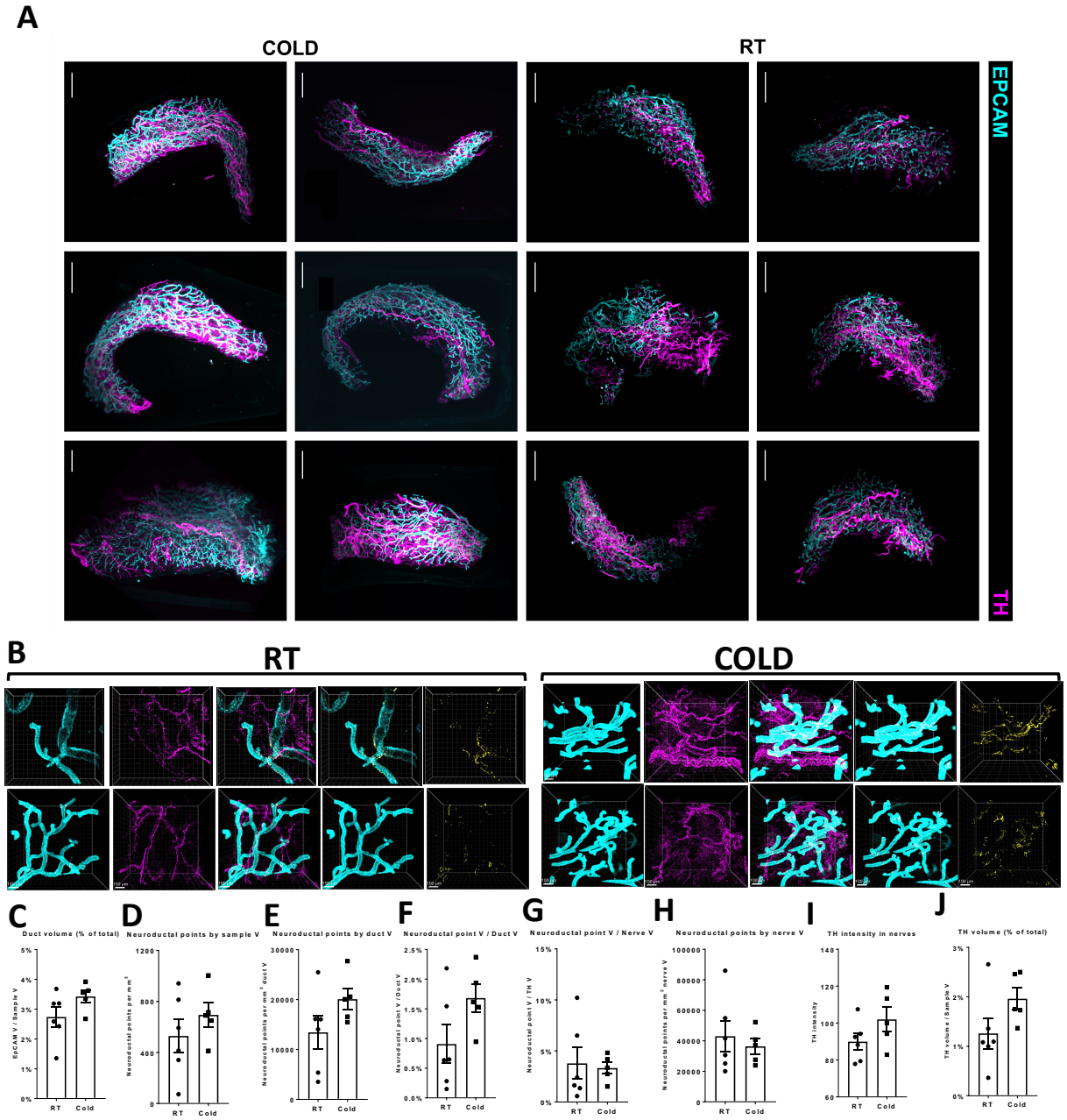

962

963 **Figure 2. SNS fibers directly innervate ductal epithelial cells.**

964 **A)** Light sheet microscopy fluorescence (LSFM) images of mgWAT isolated from female mice

965 exposed to RT or COLD for 24 hr and stained with TH antibody (SNS fibers) and EPCAM

966 antibody (ductal cells). N=6,6. **B)** Confocal images of mgWAT isolated from female mice exposed

967 to RT or COLD for 24hr and stained for EPCAM and TH antibodies. Merged staining of EPCAM
968 and TH represent neuroductal points. Representative images of 5-6 mice per condition. **C-J)**
969 Quantification of indicated parameters of images from (B). N=5-6 mice per condition.
970
971
972
973
974
975
976
977
978
979
980
981
982
983
984
985
986
987
988
989

Extended Data Figure 3

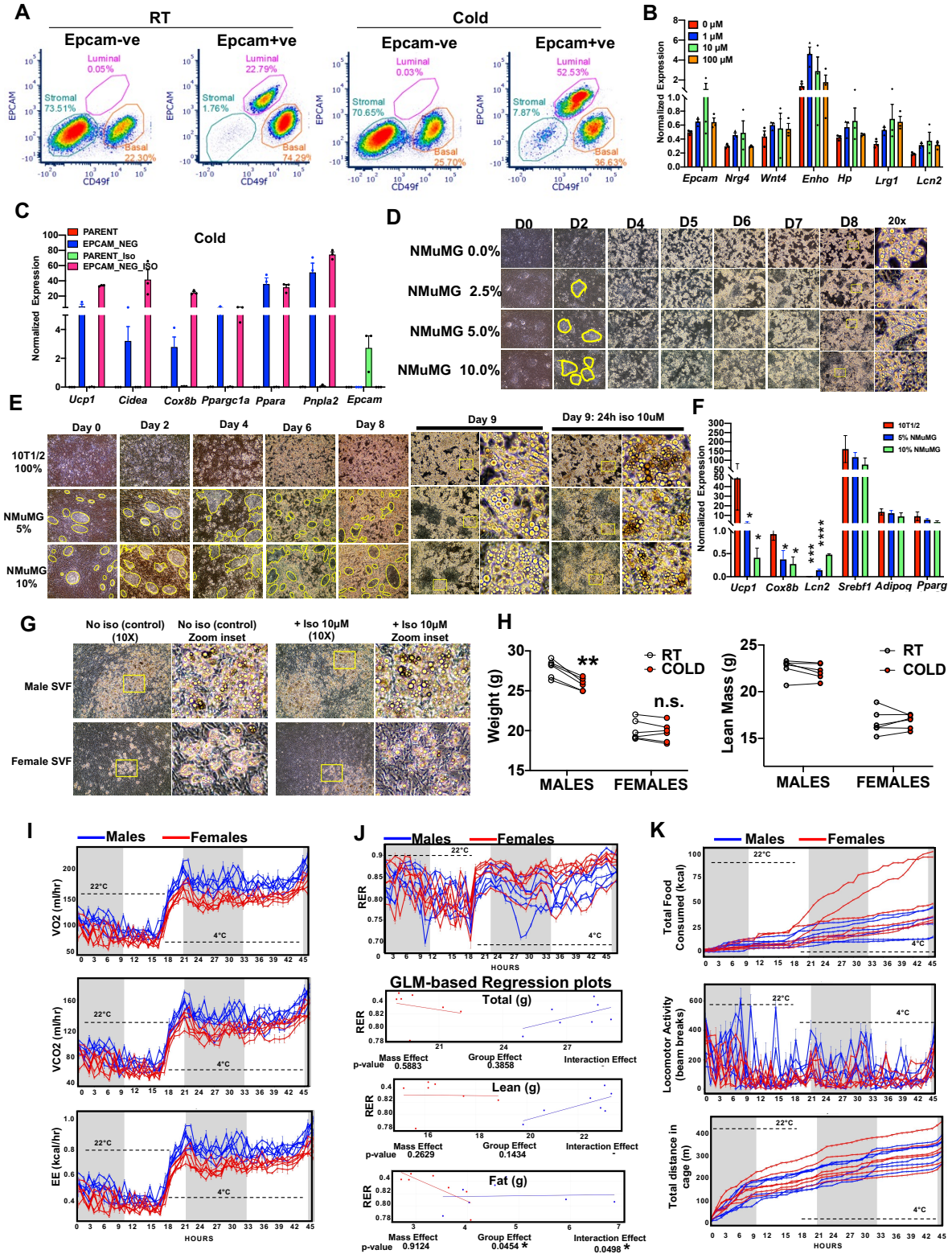

992 **Figure 3. Mammary gland epithelium inhibits cold-induced adipocyte thermogensis**

993 **A)** Representative FACS plot of CD49f and EPCAM expression in EPCAM bead selected
994 EPCAM+ or EPCAM-ve epithelial cells from RT or cold mice. 2 mice per condition and 4
995 mammary fat pads per mouse. Representative data from 4 independent experiments. **B)** Real-time
996 qPCR of indicated genes in beige differentiated SVFs from mgWAT treated with indicated
997 concentration of Iso for 5 hr. **C)** Real-time qPCR of indicated genes from beige differentiated
998 primary mgWAT SVF (Parent) and EPCAM-ve (EPCAM-NEG) cells isolated from cold exposed
999 mice treated with and without 10 μM isoproterenol (ISO) for 24 hr ex vivo. Results are from three
1000 independent experiments. **D)** Images showing cell morphology of D0-D8 beige differentiated
1001 10T1/2 and NMuMG (0, 5, and 10%) mixture cells. Yellow enclosures show NMuMG epithelial
1002 cells surrounded by 10T1/2 cells. **E)** Images showing cell morphology of D0-D9 beige
1003 differentiated 10T1/2 and NMuMG (0-10%) mixture cells. Yellow enclosures show NMuMG
1004 epithelial cells surrounded by 10T1/2 cells. **F)** Real-time qPCR of indicated genes from cells in
1005 (E). Results are from three independent experiments. *, $p<0.05$, ***, $p<0.001$. **G)** Images showing
1006 cell morphology of beige differentiated SVFs isolated from male and female iWATs. **H)** Body
1007 weight and lean mass of male and female mice before (RT) and after 24 hr cold exposure (COLD).
1008 N=6,6. **, $p<0.01$. **I-K)** Individual mice data for oxygen consumption (VO2 ml/hr), carbon
1009 dioxide production (VCO2 ml/hr), and energy expenditure (EE kcal/hr) (I), respiratory exchange
1010 ratio (RER) and generalized linear model (GLM)-based regression plots of RER with total body
1011 weight (Total), lean mass (Lean) and fat mass (Fat) as co-variates (ANCOVA) showing p-value
1012 for Mass effect, Group effect, and Interaction effect. *, $p<0.05$ (J), and total food consumed (kcal),
1013 locomotor activity (beam breaks), and total distance in cage (m) (K) of male and female mice
1014 exposed to 22°C for 21 hr and 4°C for 24 hr in Sable Promethion metabolic chambers (12 hr

1015 light/dark cycle, 45 hr total duration, white bar represents light cycle and grey bar represents night

1016 cycle). N=6,6.

1017

1018

1019

1020

1021

1022

1023

1024

1025

1026

1027

1028

1029

1030

1031

1032

1033

1034

1035

1036

1037

1038 **Extended Data Figure 4**

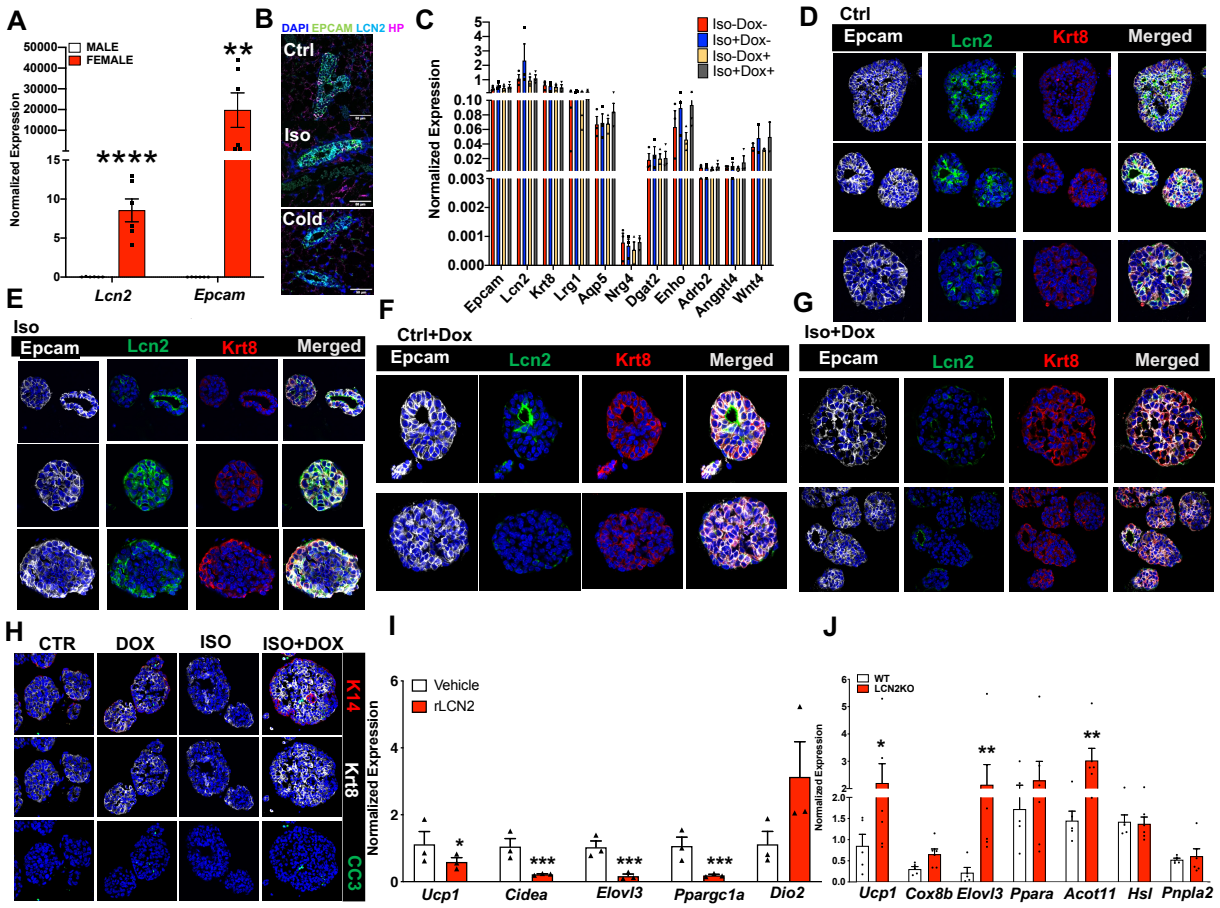

1039

1040 **Figure 4. LCN2 is a cold-induced mammokine involved in blocking cold-induced adipocyte**

1041 **UCP1 expression**

1042 **A)** Real-time qPCR of indicated genes from 24 hr cold-exposed male and female iWATs. **,

1043 p<0.01; ***, p<0.001. **B)** RNAScope FISH (see Materials and Methods) of indicated probes from

1044 mgWAT of RT or 24 hr isoproterenol or cold-exposed mice. **C)** Real-time qPCR of indicated genes

1045 in organoids derived from K8rtTA-DTA mice treated with and without ISO and Doxycycline

1046 (Dox). Results from 3 organoid experiments. **D-H)** Confocal images of immunostaining of

1047 indicated antibodies in organoids derived from K8rtTA-DTA mice treated with and without Iso

1048 and Dox. Representative images from 2-3 organoid experiments. **I)** Real-time qPCR of indicated

1049 genes from beige differentiation mgWAT SVFs derived from *Lcn2* KO mice treated with and
1050 without recombinant Lcn2 (rLcn2). *, $p<0.05$; ***, $p<0.001$ **J)** Real-time qPCR of indicated genes
1051 from 24 hr cold exposed WT and *Lcn2* KO mgWATs. N=5,5. *, $p<0.05$; **, $p<0.01$
1052
1053
1054
1055
1056
1057
1058
1059
1060
1061
1062
1063
1064
1065
1066
1067